LIGHT CURVE CHARACTERISTIC OF GAMMA-RAY BURST

By

Temam Beyan

A THESIS SUBMITTED TO

GRADUATE PROGRAMS OF
ADDIS ABABA UNIVERSITY

IN PARTIAL FULFILLMENT FOR THE REQUIREMENTS
OF THE DEGREE

MASTER OF SCIENCE IN PHYSICS

(ASTRONOMY/ASTROPHYSICS)

ADDIS ABABA, ETHIOPIA

MARCH 2024

ADDIS ABABA UNIVERSITY

PROGRAM OF GRADUATE STUDIES

LIGHT CURVE CHARACTERISTIC OF GAMMA-RAY BURST

By

Temam Beyan

Department of Physics

Addis Ababa University

Approved by the Examining Board:

Dr. Feraol Fana Dirirsa Advisor	Signature
Dr. Seblu Humne Examiner	Signature
Dr. Negessa Tilahun Examiner	Signature

Date: March 2024

ADDIS ABABA UNIVERSITY

Date: **March 2024**

Author: **Temam Beyan**

Title: **Light Curve Characteristic of Gamma-Ray Burst**

Department: **Department of Physics**

Degree: **M.Sc.** Convocation: **May** Year: **2023**

Permission is herewith granted to Addis Ababa University to circulate and to have copied for non-commercial purposes, at its discretion, the above title upon the request of individuals or institutions.

_____

Signature of Author

This Work is Dedicated

to

My be lovely family...

Table of Contents

List of Tables

List of Figures

Acknowledgements

First and for most, I want to thank Allah, the Almighty and universe's creator, for His unwavering love and concern for me. Secondly, I want to sincerely thank and appreciate Dr. Feraol Fana, my advisor, for his kindness, support, and guidance. I would like to thank all of the Addis Ababa University staff members and physics instructors. I also want to thank my friend Abel Habte for his technical and moral assistance. Finally, I would like to thanks my family, especially my lovely wife Sofia Kedir, who has been incredibly supporting me to finished this work.

Addis Ababa University
Temam Beyan
September, 2023

Abbreviations

BH	Black Hole
BNS	Binary Neutron Star
BBH	Binary Black hole
BBN	Big Bang Nucleosynthesis
BATSE	Burst And Transient Source Experiment
BAT	Burst Alert Telescope
CGRO	Compton Gamma-Ray Observatory
CMBR	Cosmic Microwave Background Radation
HETE	High Energy Transient Explorer
GRBs	Gama-ray Bursts
GBRM	Gamma-Ray Burst Monitor
ISM	Inter Stallar Medium
ICS	Inverse Compton Scattering
LGRB	Long Gama-ray Bursts
LAT	Large Area Telescope
MBH	Massive Black hole
WRS	Wolf-Rayet Star
WFC	Wide Field Camera
UOVT	Ultra Violet OpticalTelescope
SGRB	Short Gama-Ray Burst
SSC	Synchrotron Self Compton
SFR	Star Formation Rate
SN	Super-Nova
XRT	X-Ray Telescope

Physical Constants

Speed of Light	C = 2.99792458$\times$ 10^8 ms^{-1}
Gravitational Constant	G = 6.67$\times 10^{-11} Nm^2kg^{-2}$
Megaparsec	Mpc = 3.08568025$\times 10^{24}$ cm
Planck luminosity	L_0 = 10^{59}egr/s
Solar Mass	$M_\odot$ = 1.99 $\times$ 10^{33} g
Kiloparsec	kpc = 3.08568025$\times 10^{21}$ cm
Solar luminosity	$L_\odot$ = 3.839 $\times 10^{33}$erg/s
Light year	$1Ly$ = 9.46 $\times 10^{15}$m

Symbols

T_{90}	Duration of Gamma-ray burst in sec.
L	Total radaited luminosity in erg/s
τ	Time remaining before coalescence in second(s)
Γ	Bulk Lorentz factor.
$M_{\odot}$	Solar mass in kilogram (kg).
d_L	Luminosity distance from the source to Earth in Mpc
E_{iso}	Isotropic equivalent energy in erg/sec.
$\tau_{\gamma\gamma}$	Optical depth
η	Efficiency of energy conversion
α	Temporal index
β	Spectral index
θ_j	Jet opening angle
z	Redshift
t_{dis}	Energy dissipation timescale in seconds
t_{jet}	Relativistic jet launching time scale
t_{eng}	Central engine activity timescale
M_o	Mass of baryons in kg
D	Standard Doppler effect
S_γ	Total radiant energy collected in erg/cm^2/sec

Abstract

The long-lasting afterglow emissions, which shift from a higher energy X-ray band to a lower energy radio band, are produced by the interaction between the relativistic jet and the surrounding medium. Our understanding of afterglow, both theoretically and observationally, was fundamentally altered with the launch of the Swift satellite. One of Swift's observational findings was the identification of an X-ray afterglow's canonical behavior, in which the light curves generally comprise four different power law segments: initial steep decay, followed by a very shallow decay, a normal decay followed by late steep decay. Here we aimed to verify the consistency of our sampled Swift / XRT data with theoretically proposed canonical X -ray model. For this purpose, a sample of nine afterglow data randomly identified from Swift / XRT data catalogues that detected over the past ten to fifteen years. The data analysed using jupyter lab software, and various fitting parameters are generated and interpreted to justify our objectives. The results of temporal analysis show that, the dominant fraction (67%) of sampled data consistent with the shallow phase [0.5 $< \alpha_2 <$ -1] and normal phase [1 $< \alpha_3 <$ 1.5]. On the other hand, the analysis of data tells us, the majority of long afterglow GRBs (80 %) characterized by larger amplitudes, that indicates long afterglows associated with higher energy than short afterglows. Results of analysis also show, 67% of the sampled has R^2 value nearly closer to 1, which implies the data distributed about best fitting line. Similarly, correlation coefficients of all the sampled range between -0.98 and -1.00, which indicates there is a strong negative relationship between the variables, and agreed with power law decay. Error bars on the top of histograms tell the fluctuation of photons count about mean value. On our histograms, fluctuation of photons in short GRBs afterglow higher than that of long GRBs, that ensures both classes from different sources.

Key words: Gamma-ray burst, Prompt and Afterglow emission, Fireball shock internal - external shocks, synchrotron and inverse compton scattering.

CHAPTER 1

physics of gamma-ray burst

1.1 Introduction

what is gamma-ray burst?

GRBs are the brightest explosion in the Universe, arguably represent the most significant astrophysical phenomenon since the Big Bang. They detected as brief, intense and totally unpredictable flashes of high-energy gamma-rays, thought to be happened during the core collapse of super massive stars or the merger of two compact objects such as binary neutron stars or a neutron star and a stellar mass black hole [1].

The fastest extended objects in nature are known as GRBs. They can travel from a very small, compact region in a few tens of milliseconds to several minutes at cosmological distance, injecting a larger amount of energy of order 10^{54} ergs or 10^{47} joules—much more energy than the Sun will emit in its entire life of 10 billion years. The total measured fluence varies between 10^{-4} and 10^{-7} ergs / cm 2, which corresponds to an isotropic equivalent luminosity of between 10^{48} and 10^{54} erg s^{-1}. [1, 2].

Because they are relativistic events associated to the final stages of massive stars, they give insight on the properties of the host galaxy and the surrounding medium, and they emit electromagnetic radiation ranging from radio wavelengths to gamma rays, as well as potentially non-electromagnetic signals like neutrinos, cosmic rays, and gravitational waves. These attributes put GRBs at the intersection of many different fields within astrophysics. They can be identified even when they occur at great distances because of their tremendous luminosity. During explosions, ultra relativistic jets are produced accompanied by an intense gamma-ray flashes called prompt emissions that outshine all the sky at very high red shifts. Prompt

emissions often followed by afterglow signals of electromagnetic spectrum from X-ray to radio wavelengths covering time scales from tenth of seconds up to several months or more. Hence they are great interest to study cosmology [2].

As mentioned above, GRBs are characterized by radiating huge energies. A common metric for determining these energies is the isotropic equivalent energy release (E_{iso}); which is the energy that the burst would have if it emitted the energy observed by us to observers in all directions. It can be calculated from the measured fluence ($S\gamma$) as,

$$E_{iso} = \frac{4\pi d_L^2}{1+z} S_\gamma, \tag{1.1}$$

where, d_L is luminosity distance and z is red shift. Because of this, they are highly powerful cosmological tools that are complementary to other probes like galaxy clusters, stellar evolution, and supernovae (SN-Ia), which are typically characterized by the presence of a distinct (Si II) absorption line around 6150A. As a result, they can be observed up to red shift z $\sim$ 10. The most intriguing and robust property of GRBs in this regard is the correlation between intensity, isotropic equivalent energy, and spectral photon peak energy (E_{peak}). This correlation is a promising tool for measuring cosmological parameters. [2, 3].

1.2 Historical overviews of gamma-ray burst

The historical discovery and GRB research from early time to the current stages of its development classified in to five eras.

1.2.1 Early era (1960 - 1973)

Vela was USA Military satellite that was initially designed to monitor (test ban treaty) signed between countries man made radiations (explosions of atomic bombs or nuclear weapons) on earth surface, space and water body during the cold war. Series of Vela were successfully launched from 1963-1967 during the cold War to detect the hazardous events, however, July 2, 1967 unique and unusual events in signature to that of man made radiations were detected unexpectedly. Since then, this new event (GRB light curve) of astrophysical origin known as gamma-ray flash or GRB, and it was named as GRB670702 using the format GRBYYMMDD from left to right, where the first two digits represent burst year, the middle and the last two digits represent the month and the date of burst, respectively. This new event was announced to scientific community in 1973 after clearly verified that it

was not of man made radiations [4, 5].

Figure 1.1 below illustrates, the first GRB670702 light curve detected by Vela satellites with its two separate peaks identified over a duration of less than 10 seconds.

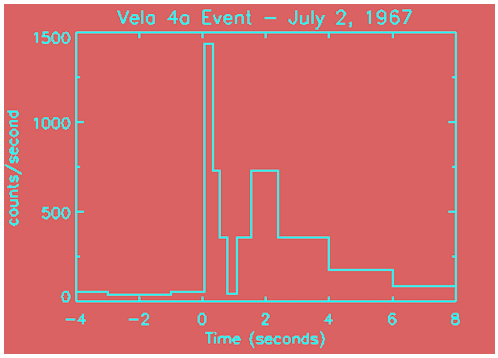

Figure 1.1: Light curve of the first GRB that Vela has ever detected. In less than ten seconds, two distinct pulses can be detected[4].

1.2.2 Dark era (1974 - 1990)

It was the era with poor detecting instruments. As a result, pace of understanding observational and theoretical properties of GRBs were slow. The three fundamental questions raised during dark era were: Where are GRBs come from? What are the source of such flashes of light? By what mechanisms do they appear in our Milky way galaxy? To answer such burning questions, series of vela launched, more than 500 GRBs data were detected. However, only a few models were proposed to explain the origin of GRBs outside the solar system, production mechanisms of GRBs, and tentative evidences showing the bimodal distribution of durations and classes of GRBs were collected as well. Furthermore, GRBs as new field of science GAMMA-RAY ASTRONOMY was opened in this era [2, 6].

1.2.3 BATSE era (1991-2000)

BATSE was the early advanced space detecting instruments that carried on CGRO, that capable to catch Gamma-ray sources from almost the entire sky in energy range of (20keV - 2MeV). In its nine years of operation more than 2704 GRBs data were collected and analysed. The Observational results of showed that, GRBs are isotropically (uniformly) distributed over the entire sky. This implies that GRBs originate at cosmological distances or from a large halo around our galaxy [6].

Figure 1.2 below, illustrates the random **isotropic distribution of 2704 GRBs** in entire sky detected by BATSE over its observation period.

It was explained that, Long duration GRBs appear in red bright bursts, while

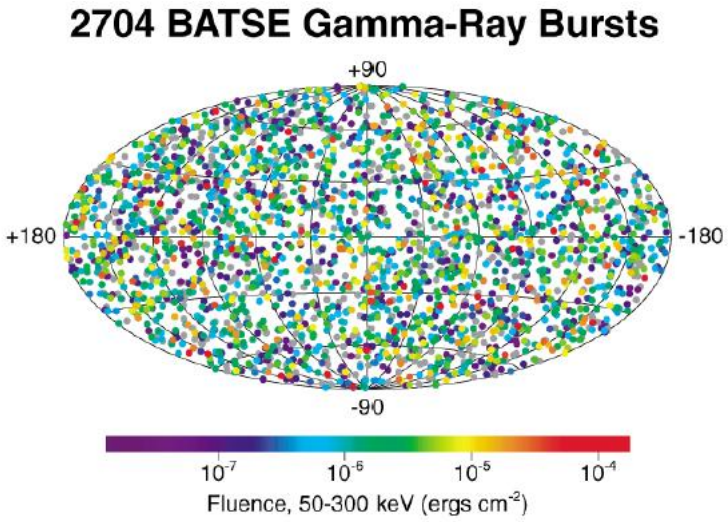

Figure 1.2: The distribution of all 2704 GRBs detected by BATSE satellite: they are clearly isotropic distribution [7].

short duration GRBs, appear in purple weak bursts, and in the bursts the grey color are those for which the fluence could not be calculated, because of incomplete data. In X- ray astronomy, fluence indicates the energy passing through a unit area [7].

The major contributions of BATSE in its nine years successful operations were:

• The apparent isotropic spatial distributions of 2704 GRBs were confirmed.

• The cosmological origin of GRBs was accepted, however debate between galactic and cosmological origin of event continued until April, 1996 [5, 7].

• Fireball model as the theoretical tool used to explain the huge amount of energy derived from observed flux and fast time variability.

• Confirm the classification of GRBs into two: (short and long GRBs) according to bimodal distribution of duration parameter T_{90}, where T_{90} is defined as the time interval over which 90% of the burst fluence is detected.

• provides clue that GRBs do not originate in our Galaxy.

• Provides database of GRBs, their spectral and temporal properties.

• The fireball model as best tool to explain the huge energy of GRBs was proposed and accepted by astronomers during BATSE era.

• BATSE observational results also revealed that gamma ray light curves are very

difficult to classify because of their diversity: (single spiky pulse, smooth with single or multiple peaks, very erratic ,chaotic and spiky). However, in the BATSE era, observations of GRBs remained limited to gamma-rays alone, since no follow-up observations at other wavelengths were possible. GRBs locations by BATSE had error-boxes of a few degrees across and thus contained a large number of possible counterparts [6, 7].

Limitation of BATSE

• Unable to classify diversities of light curves (i.e single spiky pulses, smooth with single or multiple peaks, very erratic, chaotic and spiky).

• Its observation was limited to gamma-rays alone, no other follow-up at other longer wavelengths [7].

1.2.4 BeppoSAX era (1997-2004)

BeppoSAX was an Italian - Dutch satellite next to BATSE, and launched in 1997 devoted to explore long-living afterglows from X-ray to radio wavelength. It was opened a new era for the current understanding of the mystery of GRBs. In its period of operation, the main contributions of Bepposax were:

• The existence of GRBs afterglow predicted in longer energy bands (optical-radio wave length) after prompt phase of GRBs.

• Clues of possible connection between the GRB-SN provided, and latter confirmed by HETE-2 and Swift that supporting collapser model and explosion of massive star of wolf-Rayet (WR), leaving behind BH.

• provide crucial informations on the progenitors of GRBs.

• Discovered cosmological distances of host galaxies [4, 7].

1.2.5 Swift era (2004-now)

SSOM was the third milestone satellite that opened a new era for the current development of GRB research. Nowdays, SSOM re-named as Neil Gehrels Space Observatory, after Neil Gehrels, who was high influential Principal Investigator. Swift launched November 20, 2004 and fully operational in 2005, equipped with three sensitive instruments. SSOM was dedicated to study:

• properties of prompt and afterglow phases

• progenitors (sources) of GRBs

• physical processes underlying prompt and afterglow emissions

• early evolution of universe via GRBs (the Big Bang theory), and

• non-electromagnetic phenomena, such as neutrinos, cosmic rays and GWs [4, 6].

Swift has three sensitive instruments:

• X-Ray Telescope,

• Burst Alert Telescope, and

• Ultra-Violet and Optical Telescope.

Although each of them designed for specific purpose, they are working together and enabled to study the prompt and afterglow emissions over a broad range of wavelengths [8, 9].

Figure 1.3 below, shows $Swift's$ **three sensitive** instruments.

The specific function of each instrument in detecting events described below.

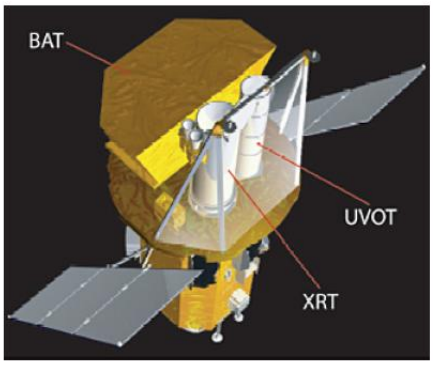

Figure 1.3: Swift Instrumentation and $Swift's$ three scientific instruments: BAT, XRT and UVOT. Figure taken from: NASA/Goddard Space Flight Centre. The size of Mask of BAT is 2.7 m^2 [7].

BAT

BAT detects GRB events and computes its coordinates in the sky and It locates the position of each events with an accuracy of 1 - 4 arc minutes with in 15 seconds. This position immediately relayed to the ground and rapid slew-ground based telescope catches the information.

XRT

It takes image and perform spectral analysis of the GRB afterglow. This provides more precise position of GRB with a typical error circle of approximation 2 arc seconds radius. The XRT also used to perform long term monitoring of GRB afterglow light curves and operated in energy range of 0.2 keV - 10 keV .

UVOT

UVOT used to detect optical afterglow and provide a sub-arc seconds position. It also used to provide longer wave length follow ups of GRB afterglow light curves.

Swift has achieved remarkable success in observing that it:
• Revealed unusual behavior in the afterglow phase of the canonical X-ray afterglow and X-ray flaring activity.
• The ability to observe the shift from prompt to afterglow emissions and detect high red shift GRBs, or the farthest distant cosmic explosions, like 050904, 080913, and 090423, was made possible.
[5, 7].

1.2.6 Fermi era (2008-now)

Compared to Swift (15keV–150keV), Fermi was designed to focus on the prompt emissions phase of GRBs by using much higher energy ranges (8keV–300keV). It is equipped with two different kinds of detectors, GRBM and LAT, on board. They offer unparalleled spectral coverage ranging seven orders of magnitudes in energy from 8 keV to 300 GeV. Significant advancements in our current understanding of the origin of GRBs were made by Fermi.
Since its launch, Fermi has made the following contributions:
• It was verified that the GRB spectra contained three elemental spectral components: a thermal component, an extra non-thermal power-law component, and a band function-like component.
• asserted that a Poynting flux-dominated flow was represented by the featureless Band function spectra that extended from keV to Gev band.
• provided an explanation for the presence of thermal components in some GRBs (such as GRB 5090902B) because of a hot fireball lacking a strong magnetization.
• The delayed onset of GeV emission in some LAT GRBs implies that during the early prompt emission epoch, there was probably a change in either the fireball's opacity or the particle acceleration condition.
• Verified that GeV emission during the prompt phase is most likely internal in origin, whereas long-lived GeV emission is most likely external. [10, 11].

1.3 Classification of Gamma-Ray Burst

Two categories of GRBs have been identified: short/hard and long/soft, based on bimodal distributions of duration T_{90} or T_{50} of prompt phase or hardness ratio. The time span during which 90% (5% - 95%) or 50% (25% - 75%) of the burst fluence or radiation is emitted in the prompt emission is known as the GRB duration, also known as T_{90} or T_{50}. A GRB typically lasts between 20 and 30 seconds for long

bursts and between 0.2 and 1.3 seconds for short bursts. [1, 3].
According to observational results, the duration of GRBs can vary over five orders of magnitude, or from approximately $\sim 10^{-2}$ s to approximately $\sim 10^{3}$ s. The two classes of GRBs—long or soft ($T_{90} \gtrsim 2$ s) and short or hard ($T_{90} \lesssim 2$ s)—have been distinguished by the bimodal distribution of T_{90}. In terms of instrumentation, T_{90} or T_{50} depend solely on the energy band and the detector's sensitivity limit. [3].

Two figures 1.4 (a) and (b) below, illustrate bimodal durations (T_{90}) distribution and the hardness ratio (HR) of two populations (long and short GRBs) that were detected by BATSE, respectively.

There are three main time scales that could be connected to the observed GRB

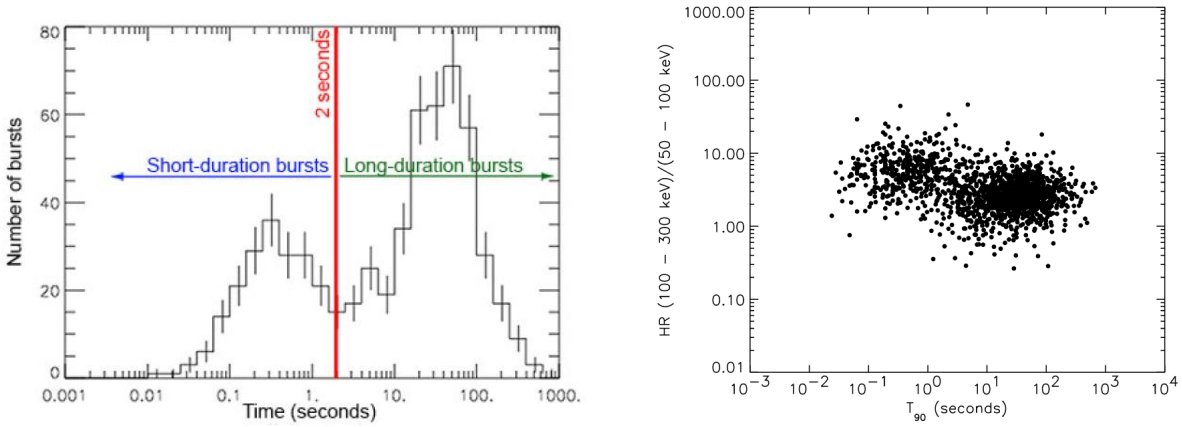

(a) T_{90} of both classes of prompt emissions

(b) HR of short to long GRBs

Figure 1.4: The bimodal duration (T_{90}) distributions of both classes are shown in Figure.1.4(a), and the T_{90} - HR diagram (Hardness ratio of short - long GRBs) obtained by BATSE for the events listed in the BATSE 4B Catalogue is shown in Figure (b). The two populations have a duration that peaks at approximately 0.3 seconds and lasts for approximately 30 seconds.The dividing line between them is approximately 2 seconds. [10].

duration, theoretically:
(1) Time scale for central engine activity t_{eng} in sec.
(2) Time scale for relativistic jet launching t_{jet} in sec.
(3) Time scale for energy dissipation t_{dis} in sec.
The observed GRB duration T_{90} should, in general, satisfy the equation:

$$T_{90} \leqslant t_{dis} \leqslant t_{jet} \leqslant t_{eng} \tag{1.2}$$

1.3.1 short or hard gamma-ray bursts

Prolonged T_{90} events, also known as hard or short GRBs, are events that last less than two seconds and make up roughly 30% of all gamma ray bursts. These types of outbursts are so powerful that they cause gravitational waves, which are rippling effects in space-time.
Short GRBs were likely caused when two ultra dense stellar masses known as neutron stars collided and formed a black hole, or when a black hole ate a neutron star. They are highly energetic and hard when compared with their long burst counter parts. For many years short-hard GRBs were not deeply researched as long GRBs. As a result, the study of short-hard GRBs was limited. However, one year after Swift launch, in 2005 a breakthrough occurred following the first detections of short hard burst (SHB) afterglows [5, 6].
The Swift observations established that SHBs are cosmological relativistic sources that, unlike long GRBs, do not originate from the collapse of massive stars, and therefore constitute a distinct physical phenomenon. One viable model for SHB origin is the coalescence or merger of compact binary systems, in which case SHBs are electromagnetic counterparts of strong gravitational-wave sources.
In this burst, the conversion of energy into gamma-rays decreases as the burst progresses. There is no radio, optical, or X-ray counterpart has found for any short burst. Short GRBs are associated with regions of little or no star formation, such as large elliptical old galaxies and located at central regions of large galaxy clusters. This rules out a link to massive stars, confirming that short events are physically differ from long events. Furthermore, they have no association with supernova [5].

1.3.2 long or soft gamma-ray bursts

Long or soft GRBs account for 70% of total observed events and have a duration of greater than 2 seconds. All long bursts display X-ray afterglow and about one-half as radio or optical afterglows. In long duration bursts energy conversion appears to remain constant through burst. Their creation linked to a young galaxies with rapid star formation and to a core collapse of powerful supernova (hyper-nova) occurred when massive stars collapsed to black hole. This realized that GRBs unambiguously associating with the death of massive stars at high red shift and originated in star-forming regions. Hyper-novas are 100 times brighter than typical supernovas and are thought to be generated by stars that are spinning particularly

fast or have an especially strong magnetic field, imparting extra energy to their combustions [6].

1.4 Global properties of gamma ray burst

Two specific global characteristics of classical GRBs began to emerge: their intensity or brightness and their angular or locational distributions. These have important implications for the origin of GRBs as well as the distance scale.

1.4.1 Intensity distribution

The brightness distribution of GRBs seemed to indicate that we were looking beyond the edge of the GRB populations; that is, there were fewer faint GRBs than would be predicted if GRBs were evenly or homogeneously distributed throughout space. The most straightforward way to measure brightness was to look at the peak flux (F, with units of [erg $s^{-1}\ cm^{-2}$]) in the GRB light curve. The brightness distribution is commonly expressed as the number of GRBs brighter than a certain peak flux F per year, denoted by N (>F). In the event that the peak luminosity (L, expressed in [erg s^{-1}]) for every GRB is identical, we could observe every GRB within a maximum distance defined by the $1/r^2$ law for a given flux F. [7, 12].

$$d_{max} = \sqrt{\frac{L}{4\Pi F}} \propto F^{-1/2}, \tag{1.3}$$

where the maximum distance, peak flux, and luminosity of the GRB source are denoted by d_{max}, F, and L, respectively. By construction, all of the GRBs at that distance would be brighter than F. The volume multiplied by the intrinsic rate (R, in units of [event yr^{-1} per volume element]) would be the number of GRBs we would detect to that brightness (or brighter) in a year: V $\times$ R $\propto$ R $\times$ d_{max}; N ($>$ F) $\propto$ R $\times$ $F^{-3/2}$. Therefore, given a homogeneous distribution, we anticipate that the number of faint GRBs, N, will increase as a power law proportional to $F^{-3/2}$, where the proportionality constant scales in a manner directly related to the intrinsic rate, R: that is, for every ten times fainter in flux, we observe, on average, approximately thirty-two times more GRBs.There was a flattening at the faint end of the brightness distribution, even though this was observed for the brightest events.

This flattening strongly suggested that we were witnessing the outer edge of the GRB distribution in space, which is a crucial hint for comprehending the distance

scale. However, without understanding the intrinsic luminosity L, we were only able to deduce the distribution's shape rather than the distance scale. It was similar to looking at a building's picture and not being able to tell if it was the life-sized building or a miniature found in a snow globe. [12].

1.4.2 Distribution in angles

There was no indication that any one direction in the sky was particularly more likely to produce GRBs than any other. Instead, the locations of GRBs appeared to be random or isotropic distribution. In the event that GRBs originated from neutron stars scattered throughout the Galaxy's disk, for example, GRB locations on the sky ought to be preferentially located on the Galactic plane (as is observed with SGRs). GRBs would have been more preferentially directed toward the Galactic center and less so toward the opposite direction if they had been associated to older stars in the Milky Way's roughly spherical bulge. Although casting doubt on some models, the inference that the Sun was roughly at the center of the GRB distribution in space allowed for a range of distance scales, from a fraction of a light year to billions of light years. [7].

1.5 Statements of the problem

Gamma-ray afterglow was discovered three decades after prompt phase. However, it has been a well studied phase than prompt phase. Especially after the launch of Swift satellite, the observational and theoretical understanding of physics of gamma-ray afterglows radically changed. Swift missions, from the very beginning aimed to detect and explain phenomenology of prompt and afterglow phase. In this regard, one of the amazing result of Swift mission was the identification of unanticipated behaviour of early X-ray afterglow- called canonical X-ray afterglow. The canonical of X-ray light curve has shown four (4) phases or segments, among which the first two phases (I and II with X-ray flares) were identified by Swift mission. The phases may have different physical origins. The temporal, spectral properties of X-ray light curves as well as its origin and the linkage with prompt phase were intensively studied by several researchers. However, there is a method and explanation gaps in analysing data and interpreting results obtained. To verify the validity of previous works that related to my work and explain unclear issues, I forward the following possible solutions.

• Do all our Swift / XRT sampled data fit with the theoretically proposed model to

describe X-rays afterglow?

• what fraction of the sampled data agreed with the model?

• Is there a causal relationships between parameters (variables) that observed?

• Are they a positive or negative correlation between parameters that generated during analysis?

1.6 Objectives of the study

General objective

The general objective of thesis is to study light curve characteristics of gamma-ray burst, there by to achieve new insight in the field.

Specific objectives

• To verify the validity of the previous work, that all X-ray afterglows did not show all their canonical behaviour.

• To calculate the fractions of our sampled Swift / XRT data that consistent with the proposed model.

• To test a causal relationships between various variables that generated during analysis of the data.

• To describe the features and implications of various parameters such as: temporal (α), amplitudes (A), standard errors and correlation coefficients (r) of analysed data.

1.7 Structure of the thesis

I'll now draw attention to the thesis's organization. The introduction included brief discussions of the background, classification (as long and short GRBs), historical discoveries, and the history of the field. In chapter 2, the emission mechanisms of the prompt and afterglow phases, as well as the theoretical and observational characteristics of both phases and their sources, would be explained by standard models. In chapter 3, the procedures, models, tools, and techniques used to collect and analyze the data will be briefly discussed. To support consistency, Chapter 4 compares the analysis results with the suggested models and explains relationships between the calculated results and the plots of the data under discussion. The last chapter will conclude with a concise summary of the work's illumination and suggestions for additional field research.

CHAPTER 2

Emission mechanism and Observational properties of GRBs

This section covered the phenomenology of GRBs, including the prompt and afterglow phases' characteristics, the progenitors of GRBs, the connection between supernovae and GRBs, and the emission mechanisms connected to each. Finally, a brief review of the power law model's canonical behavior and how it describes the X-ray afterglow's decaying mechanism.

2.1 Emission mechanism of GRBs : Fireball models

The theories or models known as the "emission mechanism" describe how the bulk kinetic energy of GRB progenitors is transformed into radiations, which in turn causes the production of new GRBs through the use of fireball models. In the early nineties, over a hundred possible models were established to explain the phenomenon of GRBs. But over time, more limited observations have led to the creation of a standard model known as the *fireball shock model*, which is able to accurately describe the properties of progenitors as well as the emission mechanisms of GRBs and afterglow. The standard theoretical model was well-organized and attempted to provide an explanation for the enigmatic GRB events over an extended period of time. [13].

2.1.1 Fireball shock model

The fireball shock model is the most effective at explaining the emission mechanism, as well as the temporal and spectral characteristics of both phases, out of all the models. A dynamic object called fireball shock makes an effort to explain the time scales that control the phenomenology of the prompt and afterglow phases. Powerful energy from over 9000 supernovae can be impressively ejected during

GRBs. The creation of this enormous amount of energy is not possible through thermal processes. What is the source of these extremely high energies? One of the few theories to have been proposed to explain why GRBs typically have such high energy levels is the fireball shock model. [13, 14].

The variability of light curves is directly related to the high energy levels because it shows that the emission of GRB energy occurs over a very small region and is in the order of 10^{52} ergs. This indicates that the emission is coming from a very small volume of space with a highly concentrated amount of radiation energy. It is then theorized that a Lorentz factor of $\Gamma \sim 100$ be associated with the GRB. To put it briefly, a fireball model that can account for all of these variables would be able to apply to all GRBs and, as a result, be a realistic model to research the physics of GRBs [14].

According to the fireball model, baryons and ultra-relativistic energy make up the optically thin fireball that contains GRB emission mechanisms. Essentially, the optical thickness and thermal profile known as the compactness problem prevent the inner engine from being detected during the GRB event. This compactness issue is resolved by the highly relativistic expansion of the fireball or (its dynamic property), which can result in a variety of shocks that produce detectable GRB and gradually fade to produce afterglows. [15].

It was Paczynske and Goodman who first proposed the relativistic fireball model in 1986. They had demonstrated that the production of electron-positron pairs $e^{-}e^{+}$ by the abrupt release of a significant amount of gamma-ray photons into a compact region can result in an opaque photon-lepton fireball. The fireball's initial energy, E_0, can be used to describe its most fundamental characteristic. Baryons M_0 (electrons with negligible mass) and $M_0 \ll E_0/C^2$ are present in the fireball, along with its mean energy per baryon, $\eta = E_0/M_0C^2$. [14, 15].

When the expanding plasma becomes optically thin, as predicted by the fireball model, radiation is released and escapes within the burst. Instead of the observed power-law (non-thermal) spectra, this mechanism would produce a quasi-thermal spectrum. It is challenging to explain the duration of GRBs with such a short time scale in such a model. Furthermore, another model called the fireball baryon load transforms all of its energy into kinetic energy rather than luminosity, resulting

in a quasi-thermal spectrum that is unable to account for the radiation emissions' efficient nature. Specifically, the emission origin associated with the two phases is produced by two different mechanisms: one is matter-dominated or particle-dominated, while the other is radiation-dominated or magnetic-dominated. The elements of the fireball model are produced when massive stars collapse or when binary neutron stars merge, and they are baryons, electrons, positrons, and photons. [10, 15, 16].

The progenitors of GRBs and the procedures for generating prompt and afterglow emissions using internal shock (IS) and external shock (ES) models, respectively, are indicated in Figure 2.1 below. When baryon acceleated within an expanding fireball of higher Lorentz factor Γ, the energy released is greater than the baryon

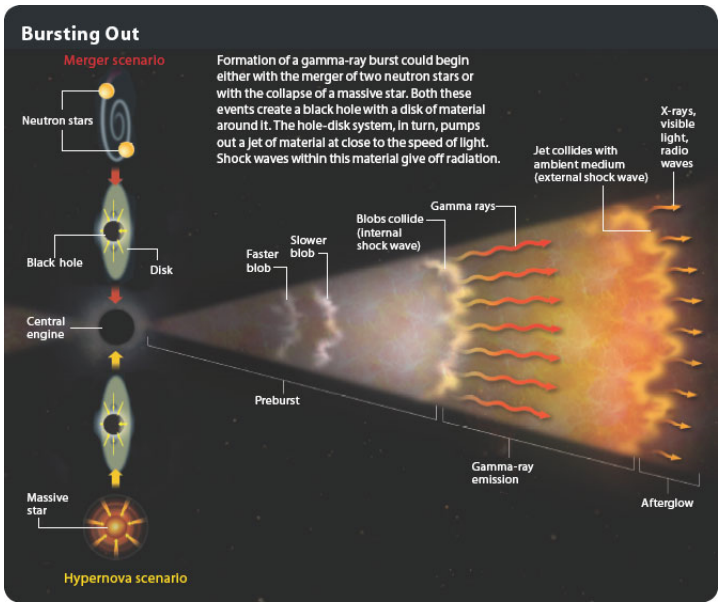

Figure 2.1: An illustration of the basic standard model's steps, complete with internal and external shocks and radiations, is provided by the fireball model visualization. Both of the primary scenarios (merger and collapser) on the left suggested that they would result in a central black hole encircled by a disk. [13].

mass in the rest frame by a factor of ~ 100. Two main results of this process are visible: at the photosphere, a portion of the thermal energy is radiated away, and the accelerated electrons create a non-thermal gamma-ray spectrum through inverse compton scattering (IC) or synchrotron processes in the internal shock at large jet radius, which results in a non-thermal gamma-ray spectrum. Rather, Poynting flux is thought to be the dominant force in the outflows that emerged

from the central engine. [10, 15, 16].
The particles involved in the fireball model experience collisionless shocks, which are caused by their acceleration and scattering as they cross the shock interaction within the Fermi process. The energy distribution that arises from this could be the kind that a power law ($\alpha \sim 2$ - 3) describes. Under such circumstances, electrons radiate non-thermally as photons through two distinct mechanisms: inverse compton scattering and synchrotron, which both reach extremely high energies (GeV bands). [16, 17].

2.2 Energy conversion processes

During GRBs emission processes in the fireball, energies can be converted from thermal form to non-thermal radiation through two different mechanisms:
1. Dissipative process
2. Radiative process
As mentioned above, both mechanisms responsible to convert bulk kinetic energy (thermal energy) in to non-thermal radiations (GRBs and its counterparts) via either synchrotron or inverse compton scattering (ICS) processes.
Dissipative process
It is the matter dominated outflows of shock waves (ejecta) from central engine that interact with itself and interstellar medium (ISM) to explain emission mechanisms of prompt and afterglow phases, respectively. There are two main dissipative shock models: (internal and external shocks) that interpret successfully the origin of emissions associated with both phases [8, 17].

A. Internal shock model
The internal shock model describes how relativistic outflows, or ejecta, from the central engine interact to create flashes of extremely energetic gamma rays. Shock waves emerge from the inner engine immediately following the first GRB event at a relativistic speed of 99.995%C, where C is the speed of light, with a value of 3×10^8 m/s, and the Lorentz factor is $\Gamma \sim 100$. As was previously mentioned, a fireball is a dynamic object made up of a mixture of charged particles (protons and electrons), photons, and magnetic fields known as plasma, in which the particles move quickly and randomly. [8].

Within the early stages of a GRB's evolution, the fireball expands radially outward

after absorbing energy left behind by the collapse or merger of compact objects close to the central engine. A number of shock waves are coming from the compact source during expansion, and they are moving at various relativistic speeds. Therefore, interaction between various shock wave fronts results in energetic emissions of gamma rays. [17, 18].

The fireball models' emission mechanism is depicted in Figure 2.2 below: There are internal and external shocks located at different points from the central engine to produce the prompt and afterglow phases, respectively. Only by means of internal shocks moving at relativistic speeds can bulk kinetic energy be converted into gamma-ray photons, which are the only known source of high energy gamma-rays. The production of inverse Compton and synchrontron emissions occurs when internal shocks interact with one another while traveling at relativistic speeds [18]

Because the shells are emitting through inverse Compton, the shock front is being slowed down, which lengthens the amount of time that multiple shock waves interact with one another. It is possible that the earlier shock waves will be released

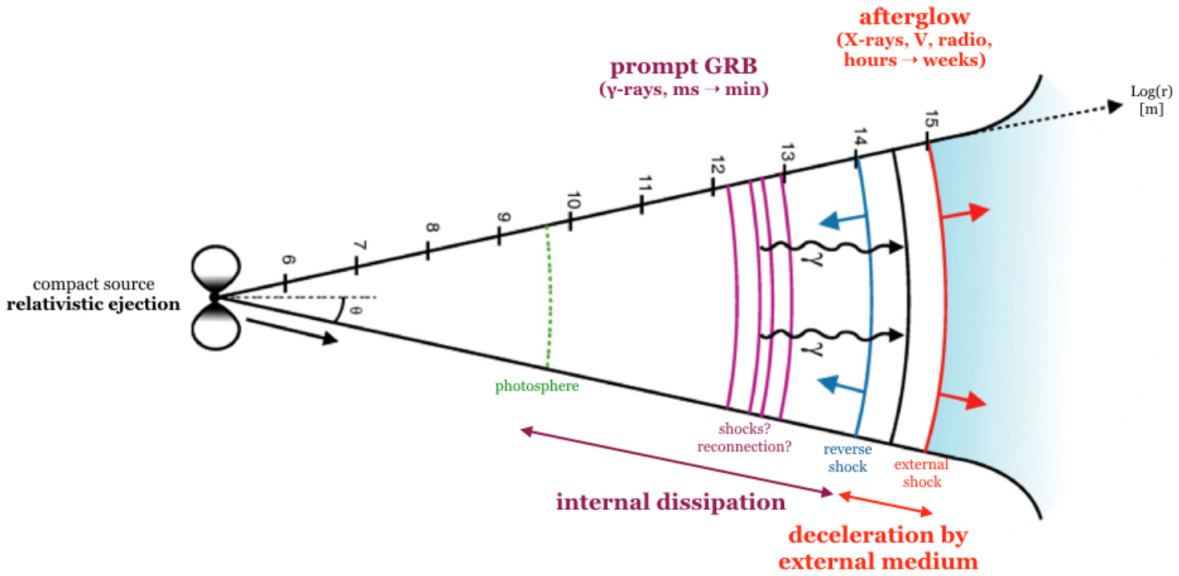

Figure 2.2: Standard fireball model [4]

more slowly than the later shock waves, which would also increase the amount of interaction between the various shock waves. [16, 18].

B. External shock model

When we talk about the external shock model, we're really talking about the internal shock waves that eventually cooled down and kept coming from the source. The length of time and wavelength of afterglow that are detected from soft X-rays using radio cannot be explained by internal shock waves. However, the emission mechanism of the afterglow, which was first observed by BeppoSAX on April 28, 1997, can be explained by external shock waves. After continuing their journey, the external shock waves will eventually come into contact with an impedance, such as a molecular cloud, within the (ISM). The phenomenon of afterglow may arise from the interaction of shock waves with either gas or dust. [19, 20].

The ISM receives the energy from the internal shock waves, which are then deposited there. This material can then become entangled in the shock front and release radiation. Since there is a lot of energy that can be deposited into the ISM due to the high energy of the shock waves at the beginning, this is what can cause the afterglow to last for so long and why it covers the entire energy spectrum. [19, 20].

Figure 2.3 below, shows different phases and associated structures that observed during collision less interaction with in ejecta (internal shock waves) and interaction of blast waves with surrounding medium (Forward and reverse shocks), respectively. A relativistic materials or jets running into external ambient medium or stellar Every time, the ejecta entered a high-density environment, producing an external shock peak in the mission. The jets may be shocked in reverse or forward direction during the external shocks. Forward shocks are produced as the material in the jet accelerates, compresses, and expands the interstellar medium. Forward shocks slow down when the rest mass energy of the swept particles equals the energy that is ejected. Deceleration length scale is set at ($\sim 10^{16}$ cm from central engine) by this. The deceleration of the material jet creates the reverse shock, which then returns to the relativistic flow. When the ejected energy is greater than the rest mass energy of the swept particles, this phenomenon occurs. [20, 21].

Radiative process

The two primary radiative models that successfully interpret the source of emission linked to both phases are inverse compton scattering and synchrotron radiation..

A. Synchrotron Radiation

When relativistic electrons spin or gyrate in a uniform magnetic field, they produce synchrotron radiation, which is an effective model for explaining the emission

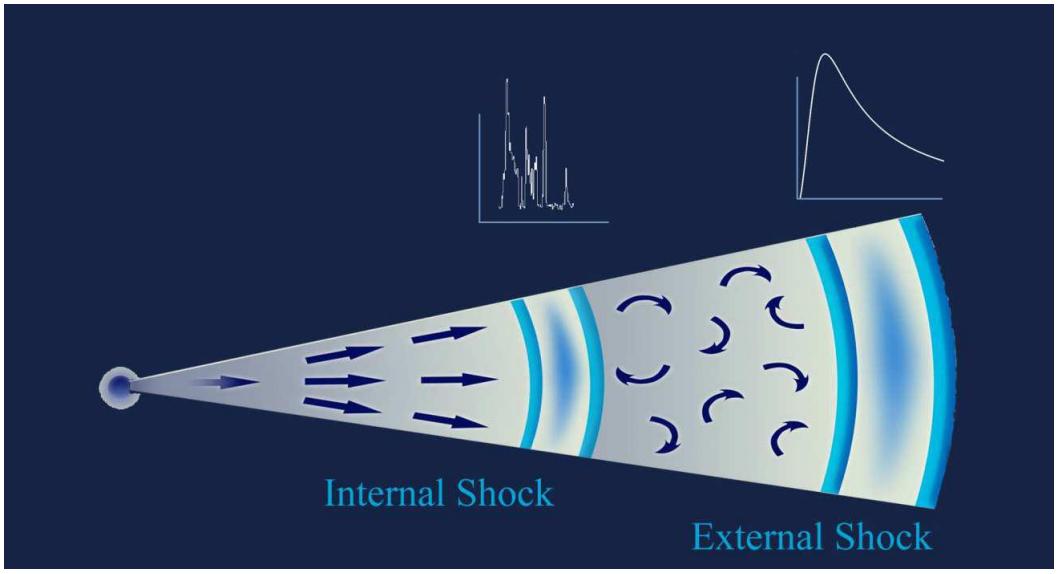

Figure 2.3: Figure illustrating the various stages or components of the conventional fireball model with both internal and external shocks. The internal shock that causes immediate emissions to continue for the duration of the central engine's operation. This is the phase that saw the formation of rapidly changing optical, X-ray, and gamma radiation. The impact of the jet with the progenitor's stellar wind, which is characterized by a smooth (but non-monotonic) light curve variation, generates the external shock that is responsible for the observed afterglow phase in radio, optical, X-rays, and γ-rays. [21].

mechanism of non-thermal radiations. It is believed to be one of the most important mechanisms behind several distinct astrophysical phenomena. Since synchrotron shock mechanism is produced by optically thin plasma ($\tau_{\gamma\gamma} \leq 1$) in a weak magnetic field, it can be used to predict the shape of the observed (non-thermal) spectra. [1, 15, 18].

This same two regimes of synchrotron emission are the fast-cooling phase and the slow-cooling phase. former describes the time scale for the electrons' cooling, which is shorter than the dynamical lifetime of the source, leading to an electron that cools more quickly than when energy is injected at a low level. The latter happens when the electron cooling process takes longer to complete than the source's dynamic lifetime. There are variations between these two regimes that are related to the radiative emission time scale. [9, 10].

The set of characteristic break frequencies in synchrotron spectra is made up of the peak (ν_m), the cooling (ν_c), and the self-absorption frequencies (ν_a). These

frequencies change over time, and their evolution is reflected in the intricacies seen in the forms of the light curves at particular energy bands. Additionally, this model is capable of accurately describing the afterglow phase. For the majority of GRBs, the optimal spectral fitting model currently thought to exist is an optically thin synchrotron spectrum. Applications of the first synchrotron model were made to the spectral fitting of GRBs [15, 22].

B. Inverse Compton scattering (IC)

Inverse Compton scattering (IC) is the result of an inelastic collision between ultra-relativistic electrons and low-energy photons. Each and every astrophysical source has a synchrotron radiation-activated SSC scattering component that allows photons from the source to be scattered to high energies and over a large frequency range. Therefore, it is acknowledged that the SSC mechanism is the phenomenon that generates high-energy emissions from GRBs and other astrophysical sources. The SSC mechanism explains the injected electron spectrum with a straightforward power-law function, despite its complexity. The SSC spectrum can be precisely described by performing an analysis of the seed photon spectrum and a complex electron energy distribution. In some cases, modeling $\approx$ 10 MeV can be used to represent the GRB spectrum as an extremely high energy SSC component. [11, 16].

2.3 Progenitors of GRBs: collapser and merger models

There are numerous ways to generate a lot of energy in the natural world. Coal power, gravitational, and rotational are a few of them. The efficiency of the nuclear model is insufficient to power a GRB. Nonetheless, the energy release of GRBs is being driven more by the later of the two progenitor models. The collapsar and merger models are shown as the primary progenitors of long and short GRBs, respectively, in Figure 2.4 below. The two models originated from the remnants of massive stars known as black holes. Direct observation is not possible due to the central engine E_0, which generates initial energy. Nonetheless, it is believed that the afterglow phase of the observed temporal structure represents the activity of the central engine, which satisfies the following features: [23].

- Able to generate a highly relativistic energy flow with $\approx 10^{51}$ to 10^{55} erg.
- Hugely variable flow leading to extremely variable light curves.

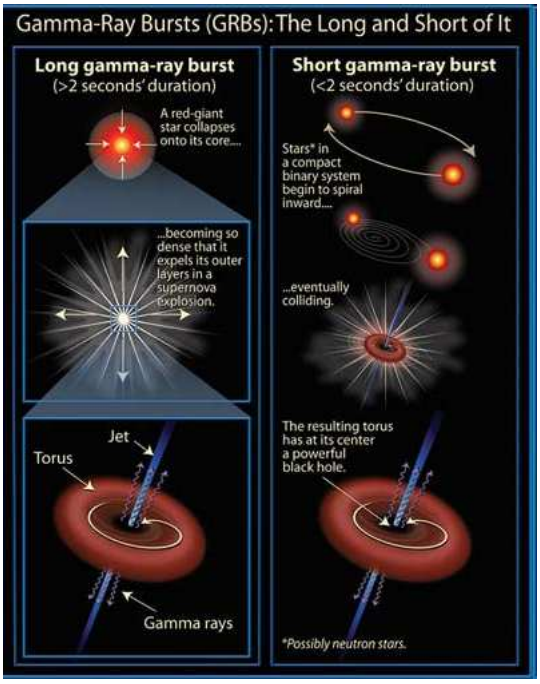

Figure 2.4: Schematic scenarios for plausible progenitors of long and short GRBs. Long GRBs come from the collapse of massive, rapidly rotating stars, while short GRBs come from the merger of compact objects [23]

- Its duration can range from a few hours to a fraction of a second.
- The potential for late-time activity to result in X-ray flares.
- Observed GRB rates suggest that this was a relatively rare event.

2.4 Supernova

Supernovae (SNe), which are incredibly powerful explosions, end the lives of some stars. Supernovae (SNe) were first studied in the early 1930s, and the first bright supernova (SN 1987A) was found in 1987. One theory explains the massive amount of energy released in supernovae ("SNe") as a result of neutron star's gravitational collapse into another star. A portion of the solar masses with kinetic energy of the order of 10^{51} ergs are expelled into interstellar space during an explosion. Heavy elements found in the ejecta are crucial for understanding the chemical evolution of galaxies, stars, and planets. Supernovae (SNe) have the potential to be sources of cosmic rays and compact remnants like black holes or neutron stars. [24].

Based on observational characteristics, supernova explosions are classified as Type I or Type II. The light curves for type I and type II supernovae are shown in Figure

2.5 below; type I supernovae are identified by the lack of a hydrogen line, while type II supernovae have a hydrogen line. Each type of supernova has its own unique light curve, but there are many variations from the general shape that are observed. These variations are caused by the unique characteristics of Type I supernovae, which arise when white dwarfs collapse and reach the Chandrasekhar limiting mass through accertion, as opposed to Type II supernovae, which are linked to the collapse of iron cores of massive stars. The evidence of hydrogen in the spectrum is a result of the large, hydrogen-rich envelopes these stars have. A supernova is categorized as Type II if its spectrum shows hydrogen lines; if not, it is classified as Type I. The Type II supernova stage has been surpassed by ancient stellar populations where no star formation takes place because massive stars evolve far more quickly than low mass stars. [24, 25]. Type I supernovae

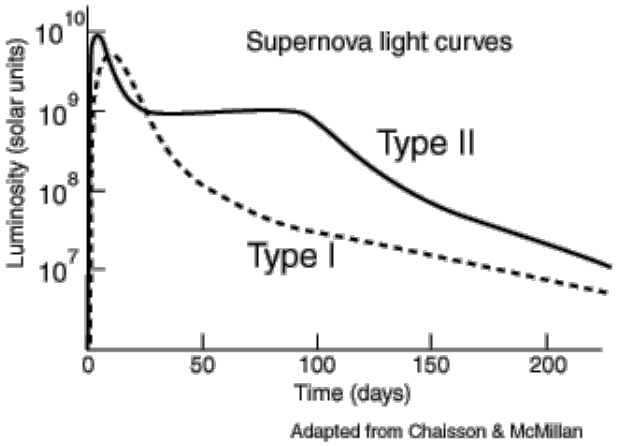

Figure 2.5: Supernova light curves of type I and type II [15].

are further classified into Type Ia, Type Ib, and Type Ic based on features seen during the early spectral explosion. The Type Ia supernovae are identified by the presence of a distinct (Si II) absorption line around 6150 A, and their late spectra display numerous lines linked to Fe emission. In contrast, the Type Ib and Type Ic supernovae lack this ionized silicon (Si II) absorption line, and they are differentiated by the presence or absence of moderately strong He I lines around 5876 A. [26].

The spectra of Type II Supernovae (SNe) can also be used to further subdivide them; these features show very broad emission lines, indicating expansion velocities of many thousands of kilometres per second, with relatively narrow features in their spectra. These are referred to as Type IIn, where "n" stands for "narrow." These could be generated by a variety of core collapse scenarios in distinct progenitor

stars, including type Ia white dwarf ignitions. However, it appears that the majority will result from iron core collapse in bright supergiants or hypergiants. The supernova is expanding into a small, dense cloud of circumstellar material, which is why the narrow spectral lines for which they are named occur. [27].

2.4.1 GRB-SN association

In the late 1990s, it was found that there were more massive supernovae that could occur (5 - 50 $\times$ 10^{44}), with energy outputs of order 10^{45} J, i.e., at least ten times larger than a common supernova, is produced at a higher rate than in typical core collapses and thermonuclear explosions. These are now often called broad lined supernovae or hyper-novae (HNe) due to their extraordinarily broad lines. Supernova 1998bw marked the first time that a GRB and SN were identified together when it was discovered to be an LGRB. The death of a massive star caused this to happen. [27, 28].

Furthermore, a lot of GRB afterglows exhibit light curve bumps that are consistent with underlying events resembling hypernovas. It's interesting to note that all GRB-SNe are currently categorized as SN Ic, meaning they have lost their envelopes covering both helium and hydrogen. A variety of events can result in the production of hyper-novae:

• While material fell back onto the neutron star core during the formation of a black hole,

• In the collapsar model, or

• In the final stages of the binary neutron star coalescence process.

All of these catastrophic events are believed to be present at the highly energetic gamma-ray burst's central engine. [27, 29].

Initially, stars with masses ranging from $25M_{\odot}$ to $90M_{\odot}$ grow to such a size that their cores become large enough to form a black hole following the formation of a neutron star from a supernova explosion, and some material will fall back onto it. This, however, diminishes the supernova's luminosity. In contrast, massive stars above $90M\odot$collapse straight into a black hole without exploding into a supernova. That being said, if the progenitor is spinning fast enough, the material that is falling produces relativistic jets, which release more energy than the initial explosion did. Not all GRBs are produced by supernovae, but in certain circumstances, these can produce them. There seems to be a connection between some binary BH and the HNe thought to power GRBs. when there is no collapse and the amount of

material is falling back smaller [29].

2.5 Observational properties of gamma-ray burst

The prompt and afterglow phases are the two primary radiative phases that make up GRBs. The former is usually observed in soft gamma-ray (10 keV to 10 MeV) radiation and lasts approximately between $\sim$ 100 ms and $\sim$ 1000 s. However, a wide range of different temporal behaviors, from single pulses to complex temporal evolution, are observed. The non-thermal emission spectrum of this prompt emission is commonly represented by a Band function, where the typical peak is located approximately at 200 keV. Alternatively, the afterglow emission is most frequently found in radio waves and X-rays and gradually disappears over time. The optical system experiences temporal fading that generally follows the form t^{-1}; however, the wavelength and burst have an impact on the fading's slope. This implies that an afterglow seen in the optical will often disappear within a week, out of the reach of the majority of ground-based telescopes. Nonetheless, there is evidence of emission in radio waves that extends from the afterglow to several months or even years following the explosion. [18].

2.5.1 Prompt phase

"Prompt emission of GRBs" refers to emission detected during the hard X-ray/gamma-ray phase, whose photons are initiating the space instrumentation and leading to multi-wavelength follow-up observations. According to the fireball model, it is thought to be the direct outflow from the central engine that deposits its gravitational energy into a thermal explosion. Put another way, prompt emission happens when kinetic energy from a catastrophic explosion event, like the merger of two compact stars or the core collapse of a massive star, is transformed into electromagnetic radiation by internal shocks that resulted from collisions between ejecta shells. [23].

That is to say, internal shocks of magnetic dissipation within the fireball effectively cause prompt emission above the pair production (photosphere at 10^{12} cm to 10^{14} cm). Either by the merger of binary neutron stars (BNS) or by the unstable accretion of matter onto a black hole, mini-shells within a jet are the source of the shocks. $\gamma \propto \Gamma$, where Γ is the bulk Lorentz factor, is where the distribution of shells is found. [22, 23].

In more detail, the expansion of fireball and the evolution of Lorentz factor

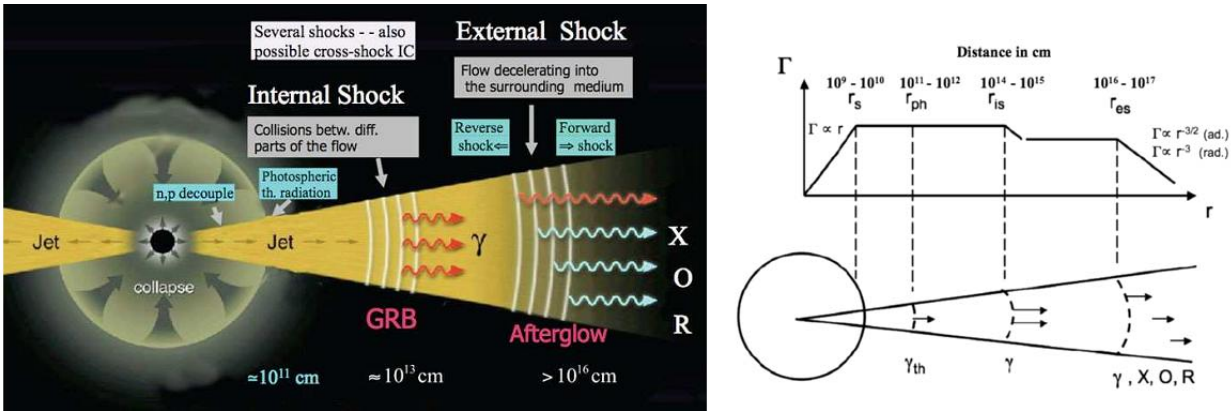

(a) Collapser model **(b)** Evolution of Lorentz factors

Figure 2.6: (Left: illustrates, the Collapser model responsible to produce prompt and afterglow phases through internal and external shocks, respectively. Similarly, the Right: shows the schematic evolution of Lorentz factor at symbolic locations of various radii.[15, 22].

explained as:

1. r_s = $\eta\ r_0$ = 10^9 - 10^{10} cm - is saturated radius, whereΓ = $\Gamma_{max} \geq$ 100 and after which it is coasting.
2. r_{ph} = 10^{11} - 10^{12} cm, where $\tau_{\gamma\gamma}$ = 1, and γ^{th} spectra formed.
3. r_{is} = 10^{14} - 10^{16} cm, where non-thermal GRB formed, and $\tau_{\gamma\gamma} < 1$.
4. r_{es} = 10^{16} - 10^{18} cm, where afterglow GRBs (from X-ray to radio bands formed), and Lorentz factor Γ decreasing [15, 22].

The prompt emission, which typically lasts a minute or less, may arise as a result of interaction within the jets and gas near the new born black hole and from collisions between shells of fast-moving gas within the jet (internal shock waves), where as afterglow emission occurs as the leading edge of jet sweeps up its surroundings (creating an external shock waves) and emits radiation across the spectrum for days, months to years, in the radio and visible light, and many hours at the highest gamma-ray energies yet observed [15].

In the region around 10^{12} cm to 10^{14} cm, the collisions between different parts of the flow is produced in different shells. As a fast shell catch up with a slower ones, they form strong internal shocks that propagates in both shells with out deceleration. Once shell became above photosphere, the heated and accelerated electrons cool

by synchrotron emission then radiation observed in γ-ray band. Each collision that occurs above pair photosphere produces a pulse in the GRB's light curves. The count rates and photon counts that the high energy detectors recorded as a function of time are represented by the GRB light curves. [22].

Every event that has been recorded exhibits a distinct variability pattern, which indicates that every light curve is unique from the others. The diversities of the light curves that the BATSE instruments detected for the prompt phase of both long and short gamma-ray bursts are shown in Figure 2.7 below. There are four distinct categories into which the light curves can be categorized:
• Single-peak events (like GRB 910711)
• A light curve that has been smoothed and is made up of multiple peaks (like GRB 920221).
• Separated multi-collisions (like GRB 930131A), and
•irregular peaks (like GRB 991216) are examples of this.
Thermal energy was eventually released at the photosphere in the form of photons as a result of the fireball expanding because of the effects of thermal pressure and then accelerating to relativistic speeds. According to the internal shock model, the dissipation occurs inside the ejecta, where the ejecta is decelerated by the surrounding medium and continues to decelerate after the internal shock phase has ceased. [6, 23].

2.5.2 Afterglow phase

Due to luck of advanced instruments, early searches were unsuccessful largely to observe the bursts position at a longer wavelength immediately after the initial burst. Once the GRB faded, deep imaging was able to identify a faint, distance host of galaxy at a location of GRB as pinpointed by optical afterglow. Afterglow gamma-ray burst studied extensively since the launch of Swift. It is the emission formed by interaction between ejected bursts and circum burst medium or interstellar gas or dust, then fading slowly at longer wavelength. Once GRB disappears, it leaves behind a counterpart at a longer wavelengths from X-ray to radio bands. Then, they are remain detectable for day or longer. As we have mentioned earlier, afterglow emissions are dominated by external shocks model [15, 22, 23].

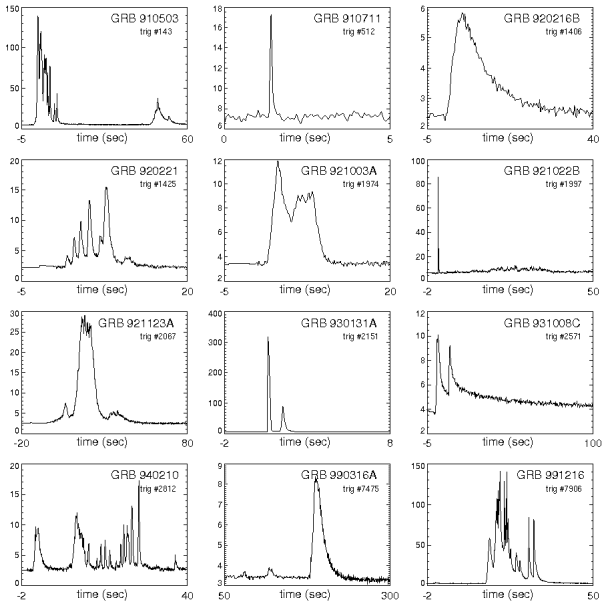

Figure 2.7: Shows the four categories of light curve diversities : (single-peak, smooth with several peaks, separated-collisions, and irregular peaks) in prompt emissions that were detected by BATSE instruments, which includes both short and long phases [28].

2.6 Theory of late time afterglows

Before Swift, late time (t $> \sim$ 10 hours) afterglow data had been collected for a moderate sample of GRBs, and observational results were generally consistent with expectations of external forward shocks and synchrotron emission models. Observational properties of late time afterglow radiations were :

• Optical afterglow, with a decay index of $\alpha \sim 1$, that exhibits a power law decay behavior of $F_\nu \propto t^{-\alpha}$. This is in line with what the conventional external shock afterglow model predicted.

• In the case of bright GRBs, a temporal break in the optical afterglow light curve is typically observed. The break time is usually approximately one day, after which there is a steeper decay with a slope of $\alpha \sim 2$. This finds resonance with the theoretical forecast of a jet break.

• The initial rise in the radio afterglow host light curve reaches a peak approximately 10 days later, after which it begins to decline. Usually, the peak indicates the passage of either the synchrotron injection frequency ν_m or the synchrotron self-absorption frequency ν_a through the radio band.

• As one would anticipate for the synchrotron afterglow model, the broad-band afterglow spectrum can be fitted with a broken power law at a fixed observer time.

• Richer features in the optical light curves have been found for bursts with high-quality data; these features include bumps and wiggles that deviate from the simple afterglow model predictions. Sharper features in light curves may be the result of energy injection from the central engine and angular fluctuations of energy per unit solid angle, while smooth bumps in afterglow light curves with duration $\delta t_{obs} \sim t_{obs}$ can be interpreted as being caused by density bumps in the external medium. [18, 24, 25].

2.7 Theory of early X-ray afterglow

The canonical behavior of X-rays (which have different shapes) in the first few hours after a prompt phase (GRB), which the Italian Beppo-SAX missed, was one of the amazing discoveries made by Swift. Several remarkable features of the early X-ray light curves were discovered through quick observation. The canonical behavior of many early X-ray light curves is actually as shown in Figure 2.8 below, in which there are three distinct power-law segments (marked I, II, and III) and, in some cases, a jet break at a later time (IV). Long after the prompt phase (10^2 - 10^4 s) has ended, about half of the GRBs exhibit bright flares in the X-ray light curves. Under certain extreme circumstances, the integrated energy of these flares can complement or exceed the initial burst of gamma-rays, posing a severe risk to the suitability of current theoretical models. [26]. Following the end of GRB, the afterglow phase was seen at all wavelengths, including radio, optical, infrared, and X-ray. The shortest signal among these is the X-ray afterglow, which emerged first and is the strongest (having the highest frequency next to the $\gamma - ray$). In actuality, it appears to have started while the GRB is in progress. An X-ray light curve that is observed a few hours following the burst can typically be extrapolated to the later stages of the prompt emission. Owing to its minimal fluctuation and extended recorded duration (ranging from minutes to weeks or longer following the GRB event), an official X-ray light-curve for the afterglow was established using the data from the Swift / BAT-XRT instruments. [27].

The four segments are associated two by two as: phases (I, II) and phase (III, IV), with their corresponding temporal indices, are identified as early afterglow and late time afterglows, respectively. Segment I and II with x-ray flares phase (V), were identified by Swift, while the other two phases were identified in pre-Swift era. The canonical X-ray afterglow phases are I, II, III, and IV, which are

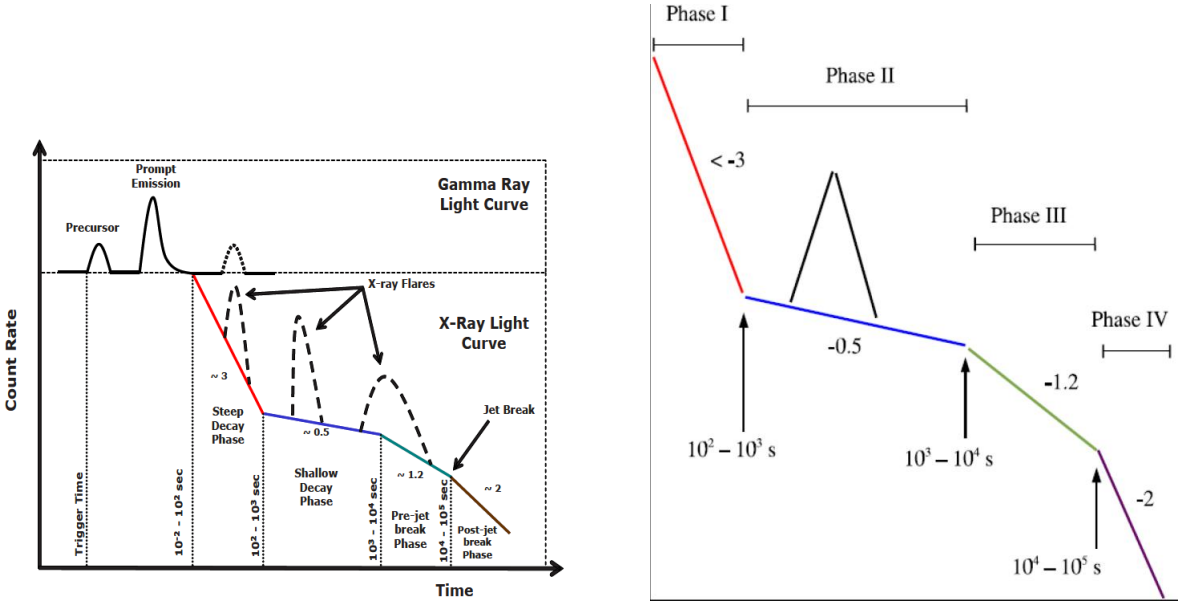

(a) GRB and X-ray light curves

(b) Canonical Segments of X-ray light curves

Figure 2.8: Left: Canonical GRB light curve, illustrating the prompt phase and afterglow phases. Right: Canonical X-ray light curves show the following components: a standard afterglow phase (pre-jet break phase), a jet break and post-jet break phase, and a steep decay phase (typical index of 3) that can break to a shallower decline. Occasionally, an X-ray flare is observed. [18, 23].

also referred to as early steep decay, shallow decay or plateau phase, normal decay phase, and late steep decay phase, respectively. This is represented in Figure 2.8 above. The first and most frequently observed component is an early steep decay indicated by solid lines; the other two components, indicated by dashed lines, are only occasionally observed in a fraction of bursts. The portion that I believed to be connected to the prompt phase occurs while the central engine is still running; the remaining afterglows are caused by the dynamics of the interaction between the jet and the surrounding medium. [30, 31, 32].

2.7.1 Early steep decay of X-ray afterglow light curves

Early afterglow GRBs were found in the swift mission less than a hundred seconds after the trigger. The early steep decay phase is the tail of prompt emission that is governed by the curvature effect, whereby light propagation effects cause emission from various viewing angles to reach the observer with varying delays [33]. The correlation between the spectral index β and temporal index α of higher latitude emission is described as follows:

$$\alpha = 2 + \beta \tag{2.1}$$

It is independent of any of the environmental or other parameters such as peak frequency and cooling frequency that influence the closure relations for the external shocks [34]

Swift answer the debate of separation between prompt emission and afterglow regarding to internal and external origin of the prompt emission i.e internal shocks are the origin of prompt emission, where as external shocks of afterglow. [33, 34]. Figure (2.8) above illustrates the early steep decay's slope, which is approximately $3 < \alpha_1 < 5$. It is the phase that could be associated with high latitude emission linked to the prompt gamma-ray sources at R $\gtrsim 10^{15}$ cm. When the central engine shuts off before the X-ray light curves start to decline, it is observed. Conversely, in the event that the emission region, or CE, is located at a radius significantly smaller than the rapidly declining X-ray light curve, the central engine becomes active and dependent on time. A thorough analysis of a sample of GRBs indicates that the early steep decay phase can be explained by the high latitude curvature effect model. [35, 36, 37].

The achromatic change in phase for the sample GRBs, as shown in figure (2.8), signifies the transition in the light curves. The power law decay relation $F_\nu \propto t^{-\alpha}$ was followed by these GRBs, where α_1 = 2 + β for the curvature effect model. In general, this phase has already remained within the time intervals shown previously in figures (2.8) (a) and (b) of 10^{-2} - 10^2 seconds and 10^2 - 10^3 seconds.

2.7.2 Plateau/shallow decay and X-ray light curve

The shallow phase, also known as the plateau phase, is distinguished by a very small decay with a decay index value of [$0.5 < \alpha_2 < 1.0$]. When the energy is released to the external shock that has slowed down, it rises. Nevertheless, the transition to phase III (normal decay) occurs when the energy is terminated, causing the light curves to decay more slowly. During this stage, the X-ray and optical bands' light curve shapes should resemble each other, with breaks occurring in both bands at the same moment. [38, 39].

Two plausible theories can be offered for the shallow/plateau phase:(1) The decrease of the Lorentz factor Γ at the end of prompt emission results in a smooth and gradual injection of energy into the forward shock. Based on the energy injected and Lorentz factor, the mass injected to the forward shock is determined. Consequently, the Lorentz factor Γ rises monotonically with radius, where the flux decays according to a power law and is dependent on the injected mass and energy. [40, 41].
(2) The source's central engine continues to run for hours following the explosion, injecting smooth and continuous energy at later times, multiple times following the explosion. The X-ray plateau was caused by the prompt X-ray emission that was dispersed throughout the host galaxy by dust. [41, 42].

2.7.3 X-ray light curve normal decay

The canonical X-ray afterglow decays normally, with a decay index of approximately [$1.0 < \alpha_3 < 1.5$], as predicted prior to Swift and in line with the standard fireball afterglow model in the ISM. The conclusion of the energy injection at the external forward shocks is relevant to its explanation. This circumstance arose when: (1) The Lorentz factor is decreasing to the point of minimality, which carries a sizable initial energy in forward external shock waves. (2) There must be no movement from the central engine. Generally speaking, the conventional forward shock model predicts a normal decay. [43].

2.7.4 X-ray light curves: late steep decay after the plateau

Figure 2.8 illustrates the late steep decay phase, with the decay slope of index $\sim$ -2 and the decay represented at the left side. Following the standard decay, a continuous jet from a long-lasting central engine powers the X-ray emission. Then, beneath emission, there is X-ray flux from the external shock. In fact, the accretion history of the collapsar model can be matched with the canonical X-ray light curve. The relationship between the X-ray luminosity and the central engine's accretion power. The late steep decay observed by Swift is indicative of an achromatic steepening resulting from jet breaks. The ejecta are collimated into a jet break when their Lorentz factor increases above θ_0^{-1} in relation to the jet opening angle θ_0. Ultimately, a jet break is anticipated during this phase in the forward shock model. One theory regarding jet breaks is that they result from GRB emission beaming. There are two jet breaks in this phase: pre-jet and post-jet. (see Figure 2.8) [44, 45]

2.7.5 Time breaks in swift X-ray afterglow

There are three break points and the time at that points are called breaking time of afterglow light curves. They are the first break time ($t_{break,1}$), the second break time ($t_{break,2}$), and the third jet break time ($t_{break,3}$) [45].
Each time break shows when the phase of light curves changes from one phase to the next phase. As illustrated in figure 2.8 (a) and (b), they can be defined as:
$*$ $t_{break,1}$ is around $t_{break,1}$ (10^2 - 10^3) s $< t_1 <$ $t_{break,2}$ (10^3 - 10^4) seconds.
$*$ $t_{break,2}$ is around $t_{break,2}$ $(10^3 - 10^4)$ s$< t_2 <$ $t_{break,3}$ (10^4 - 10^5) seconds.
$*$ $t_{break,3}$ is around $t_{break,3}$ (10^4 - 10^5) s $< t_3$ seconds.
The time at which the slowly decaying emission from the forward shock becomes dominant over the rapidly decaying flux from the prompt emission at a large angle is also indicated by the first break time ($t_{break,1}$). At t $> t_{break,1}$, the prompt emission initially predominates over the external shocks in a sharply decaying flux. [45].

2.8 Flux decay of X-ray light curves

The fluence (S_γ) is the total radiant energy collected from the GRBs per unit area over the duration of the event (i.e, T_{90}). It is computed by integrating its energy flux over time and the energy range of the detector (i.e, the total energy collected

per unit time and per unit area). The fluence measured between energiesE_{min} and E_{max} is given by[28]

$$S = T_{90} \int_{min}^{max} E \frac{dN}{dE} dE, \tag{2.2}$$

and the energy flux of a burst is also defined as,

$$F = \int_{min}^{max} E \frac{dN}{dE} dE. \tag{2.3}$$

The flux decreases quickly with time when a relativistic, conical, and optically thin source moving with a Lorentz factor Γ abruptly turns off [47]. When a source of this kind with a spherical coordinate (r, θ, φ) is specified, the source turns off at r = R_0. as shown in figure 2.9 below, where r is the radius of the photons or jets, R_0 is the observer's radius, and θ is the angle measured with respect to the observer's line of sight. The time dependence of observed flux follows from the

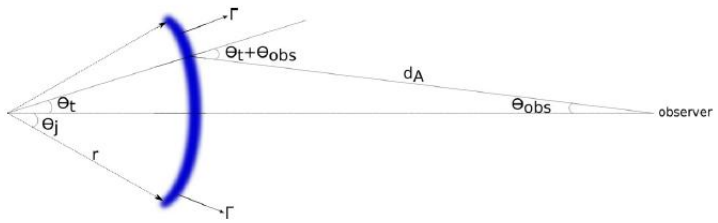

Figure 2.9: A sketch of the various angles and distances for the large angle (or high latitude) emission when the γ -ray source turns off suddenly [18]

Lorentz transformation of specific intensity. With respect to the relativistic source of the moving object with specific intensity $I_{\nu'}$ and spectrum frequency f $\propto \nu'^{-\beta}$, the specific flux in the observer frame is,

$$f_\nu(t_{obs}) = \int d\Omega_{obs} I_\nu cos\theta_{obs}. \tag{2.4}$$

where I_ν is the specific intensity of the source photon at constant frequency and $d\Omega_{obs}$ is the source's solid angle. In order to determine the standard flux decay of GRBs, we must first define I_ν and $d\Omega_{obs}$ in the relativistic beaming. The transverse component of momentum in a relativistic photon beam remains constant under Lorentz transformation, meaning that its comoving and lab frame values remain unchanged. [18, 30]. Thus,

$$\nu sin\theta = \nu' sin\theta', \tag{2.5}$$

or

$$sin\theta = \frac{\nu'}{\nu} sin\theta'. \tag{2.6}$$

Since the photon frequency on the observer frame, ν, can be expressed using the standard Lorentz transformation of photon as, in terms of the comoving frequency, ν'

$$\nu = \frac{\nu'}{\Gamma(1 - \frac{\upsilon cos\theta}{c})} = \nu' D, \tag{2.7}$$

where D is standard Doppler effect which is expressed as $[\Gamma(1 - \frac{\upsilon cos\theta}{c})]^{-1}$. The ratio and substituting this ratio in to Equation (2.6), we obtain,

$$sin\theta = \frac{sin\theta'}{D} \tag{2.8}$$

For large Γ, $\theta \approx \frac{\theta'}{\Gamma}$. The angular size of the photon beam in the lab frame is smaller than it is in the co moving frame by a factor of $\sim \Gamma$, indicating that photons are focused in a forward direction. Additionally, there is a Γ^2 factor difference in the solid angle for a canonical photon beam in the lab frame compared to the comoving frame. This suggests that the solid angle's Lorentz transformation, which is defined by [18].

$$d\Omega = sin\theta d\theta d\phi = \frac{sin\theta' d\theta' d\phi'}{D^2} = \frac{d\Omega'}{D^2} \tag{2.9}$$

The particular intensity (I_ν) is the other parameter in the Lorentz transformation. It is described as the flux per unit frequency and the solid angle carried by the photons that are traveling in a narrow conical beam that has its axis perpendicular to the surface dA. Thus,

$$I_\nu = \frac{dE}{d\nu dt_{obs} dA d\Omega}. \tag{2.10}$$

Given that $d\nu' dt'_{obs} dA'$ = $d\nu dt_{obs} dA$ is Lorentz invariant, equation (2.9) and E = $\Gamma E'$ can be reduced to equation (2.10).

$$I\nu = D^3 I'_{\nu'}. \tag{2.11}$$

Since for intrinsic spectrum , $I'_\nu = I'\nu'^{-\beta}$, where β is spectral index, then the specific intensity is summarized as,

$$I_\nu = D^3 \nu'^{-\beta} I'. \tag{2.12}$$

This equation, can be simplified by substituting the value of $\nu'$from equation (2.7),

$$I_\nu = D^{3+\beta} \nu^{-\beta} I.' \tag{2.13}$$

Finally, substituting equation (2.9) and equation (2.13) in to equation (2.4) and integrating over $d\phi$ in the interval $0 - 2\Pi$, the observed flux becomes,

$$f_\nu(t_{obs}) = 2\Pi \int d\theta_{obs} \frac{I'_\nu \nu_0 sin2\theta[(1+z)\Gamma]^{-(3+\beta)}}{2\nu^\beta (1 - \upsilon cos(\theta + \theta_{obs})/c)^{3+\beta}}, \tag{2.14}$$

where the frequency that falls on the power law spectrum segment for $I'_{\nu'}$ is denoted by ν'_0. The diagram in Figure (2.8) allows us to apply the sine law to determine that $\frac{sin\theta}{dA} = \frac{sin\theta_{obs}}{R_0}$. This implies that $sin\theta_{obs} = \frac{R_{0sin\theta}}{dA}$, and when we substitute this into Equation (2.13), in the case $\theta_{obs} \ll \theta$, yields [13, 18].

$$f_\nu(t_{obs}) = 2\Pi I'_0 \nu'_0 \nu^{-\beta}[(1+z)]^{3+\beta}(\frac{R_0}{dA})^2 \int_{\theta t}^{\Pi/2} d\theta \frac{sin\theta cos\theta}{(1-\upsilon cos\theta/c)^{3+\beta}}. \tag{2.15}$$

Using substitution methods of integrating , the equation can be simplified as,

$$f_\nu(t_{obs}) \propto [(1-\frac{\upsilon cos\theta}{c})]^{-(2+\beta)\nu^{-\beta}}. \tag{2.16}$$

A photon emitted at r = 0, is delayed in arriving at the observer frame compared to photons released at ($r = \upsilon t$, θ, and φ).

$$t_{obs} = t - \frac{\upsilon cos\theta}{c} = t(1-\frac{\upsilon cos\theta}{c}) = t/\Gamma D. \tag{2.17}$$

From this equation , the relation between t_{obs} and D is $t_{obs} \propto D^{-1}$. Then the flux decay with time of observed light curves from equation (2.16) is summarized as,

$$f_\nu(t_{obs}) \propto t^{-(2+\beta)}\nu^{-\beta}. \tag{2.18}$$

The standard convection of flux decay is,

$$f_\nu(t_{obs}) \propto t^{-\alpha}\nu^{-\beta}, \tag{2.19}$$

where α = $2+\beta$

2.9 Calculating luminosity of X-ray afterglow

Luminosity is the total amount of electromagnetic energy radiated (out put) by an object per unit of time. The observed isotropic-equivalent luminosity in the X-ray afterglow, L_x can generally be expressed as,

$$L_x = \int_{\nu 1}^{\nu 2} L_\nu(t) d\nu, \tag{2.20}$$

where $L_\nu(t)$ = $\frac{4\Pi d_L^2 F}{(1+z)}$, substituting $L_\nu(t)$ into equation (2.20) reveals:

$$L_x(t) = \frac{4\Pi d_L^2}{(1+z)} \int_{\nu 1}^{\nu 2} \frac{F_\nu}{(1+z)[(1+z)t]d\nu}, \tag{2.21}$$

The luminosity distance is denoted by d_L. The spectral frequencies in the energy band are ν_1 and ν_2, the red shift is denoted by z, and the spectral luminosity at the source's cosmological frame, $L_\nu(t)$, is measured in the frame. [46, 47]

$$L_x(t) = 4\Pi d_L^2 \int_{\nu 1/(1+z)}^{\nu 2/(1+z)} F_\nu[(1+z)t]d\nu, \tag{2.22}$$

Because $F_\nu(t)$ is assumed in standard form and measured in the observer frame, Equation (2.22) can be simplified to:

$$L_x(t) = 4\Pi d_L^2 (1+z)^{(\beta-\alpha-1)F_x(t)}, \tag{2.23}$$

where $F_x(t) = \int_{\nu 1}^{\nu 2} F_\nu(t)$. Here, we have understood that the flux decay of afterglow light curves are governed by standard power law of model, i.e $f_\nu(t_{obs}) \propto t^\alpha \nu^{-\beta}$, where $\alpha = 2 + \beta$. This is a theoretical understanding for the afterglow era. Therefore, swift observation have led to the better understanding of x-ray afterglow light curves for the initial few hours. The two mechanisms of emission have related to the behaviour of central engine of the burst. Now let us introduce the method and material used to analyse the temporal and spectral indices of canonical X-ray afterglow light curve in the next chapter.

CHAPTER 3
Research Methodology

3.1 Research designs and methods

In this section, the approach, methods and model used to perform our thesis, data collection techniques and analysing processes using python 3 programming language will be discussed briefly.

3.1.1 Models

To address our objectives mentioned earlier, confirmatory and explanatory research approach followed. Methods and models as well as statistical tool that agreed with our sampled data applied.

Power law Model.

The conventional fireball model defines the canonical behavior of X-ray light curves as being characterized by a straightforward power law model.

$$f_\nu(t) = At^{-\alpha}, \tag{3.1}$$

where α, the temporal indices (slopes) and subscripted by numbers 1, 2, 3, and 4 for early steep decay, shallow or plateau decay, normal decay, and late steep decay, respectively, that were captured by the Swift / XRT, and f_ν, the X-ray flux (light curves) decay, as a function of time.

3.1.2 Numerical models

R-squared, Covariance, and correlation coefficients.

R-squared (R^2) - is the "percent of variance explained" by the model. By the same token, it is the fraction by which the variance of the errors is less than variance. The values of (R^2) ranges from 0 to 1 and typically expressed in percentage, and

defined by the equation:

$$R^2 = \frac{SSR}{SST} = \frac{\sum(\hat{y}_i - \bar{y})^2}{\sum(y_i - \bar{y})^2}, \tag{3.2}$$

where SSR - is the sum of square regression or the sum of square residuals.
SST - is the total sum square / sum square total.
$\hat{y}$ - is the prediction or points on the fitting line.
$\bar{y}$ - mean of all the values.
y_i - is the actual values / points.
R - squared can also be defined as,

$$R^2 = 1 - \frac{\sum(\hat{y}_i - y_i)^2}{\sum(y_i - \bar{y})^2}. \tag{3.3}$$

The characteristic of light curves of X -ray afterglows determined by dispersion of variables (numbers of bursts versus time in space). In particular, the directional and degree of relationship between two dimensional data can be explained by statistical tools: covariance and correlation coefficients, respectively.
The covariance of sampled data defined by,

$$C(x, y) = \frac{1}{n-1}\sum_{i=1}^{n}(x_i - \bar{x})(y_i - \bar{y}) \tag{3.4}$$

If covariance of the sampled data known, then correlation coefficient r_{xy} can be calculated as,

$$r_{xy} = \frac{C(x, y)}{\sqrt{v(x)v(y)}} = \frac{1}{n-1}\sum_{i=1}^{n}\frac{(x_i - \bar{x})(y_i - \bar{y})}{sd(x)sd(y)}, \tag{3.5}$$

where cov(x,y) is covariance, sd(x) and sd(y) are standard deviation of x-data and y-data and they are square root of variance v(x) and v(y), respectively. The values of covariance lies between the range + ∞ and - ∞, where as the value of correlation coefficient r_{xy} limited between range -1.00 and +1.00. where, x-data and y-data represent time in seconds and X-ray flux in erg / cm^2), respectively.

3.2 Data sources and sampling methods

Data sources

For our work, we used the existing primary data source from Unite Kingdom Swift Science Data Centre (UKSSDC), that was detected by Swift / XRT over the past 10 to 15 years ago. In our sample, both the classes (short and long) of gamma-ray bursts are included.

Data sampling technique and size

Three Criterion were designed to select the required sample: i.e class of GRB

afterglow, the number of light curve breaks and well defined red shifts (z) are used to select the samples. Accordingly, nine (9) GRBs afterglows are selected using simple random probability sampling method. The sampled GRBs afterglow tabulated below.

Table 3.1: shows Swift / XRT sampled X-ray afterglow data.

Table 3.1: Shows sampled data that taken from Swift / XRT data catalogue.

Type of GRBs	One LC break	two LC breaks	total
Short	3	1	4
Long	3	2	5

3.3 Data analysis

In order to extract relevant parameters that used to describe our work, we use Jupyter lab and python 3 programming language to analyse our sampled data. The results of analysis summarized in next section using tables and plots to discuss.

CHAPTER 4
Results and discussion

4.1 Results and discussion of fitting parameters

Analysing our sampled data, the values of various fitting parameters extracted to compare and interpret the obtained results with the theoretical model. In table 4.1 below, the results of temporal indices and amplitudes are summarized to discuss.

I. Temporal indices (slope)

Table 4.1: Shows the results of data analysis: to extract fitting parameters, temporal indices (α) and amplitudes (A) for both phases of the sampled.

GRBYYMMDD	Class	$T_{90}(s)$	z	$Lc_{break(s)}$	α	A$\times 10^{-8}$
GRB140614A	long	233.90	4.23	2	-$1.78^{+0.09}_{-0.09}$	$(4.81^{+2.27}_{-2.27})$
GRB130701A	long	4.38	1.16	1	-$1.55^{+0.64}_{-0.64}$	$(1.87^{+0.55}_{-0.55})$
GRB121128A	long	23.30	2.20	2	-$1.50^{+0.09}_{-0.09}$	$(1.69^{+0.73}_{-0.73})$
GRB150314A	long	14.79	1.76	1	- $1.19^{+0.03}_{-0.03}$	$(1.43^{+0.18}_{-0.18})$
GRB051221A	short	1.40	0.55	2	-$1.17^{+0.07}_{-0.07}$	$(5.10^{+0.17}_{-0.17})$
GRB130418A	long	>300	1.22	1	-$0.78^{+0.05}_{-0.05}$	$(0.01^{+0.01}_{-0.01})$
GRB140903A	short	0.30	0.35	1	-$0.67^{+0.06}_{-0.06}$	$(0.15^{+0.05}_{-0.05})$
GRB190627A	short	1.60	1.94	1	-$0.63^{+0.04}_{-0.04}$	$(0.55^{+0.12}_{-0.12})$
GRB090510	short	0.30	0.90	1	-$0.33^{+0.05}_{-0.05}$	$(0.02^{+0.01}_{-0.01})$

As mentioned in table 4.1 above, the majority of long GRBs, except LGRB130418A with $T_{90} > 300$ sec associated with greater temporal indices, indicating that long GRBs originated from death of massive stars or collapsers. The magnitudes of temporal indices (α) related to the activities and life time of central engines. The steeper the fitting curves, the greater magnitude of temporal indices (α), then the faster X-ray flux decaying. On the other hand, the flatter the fitting curves, the smaller temporal indices, then the slower X- ray flux decaying. In our case, X-ray flux produced by long GRBs sources (supper massive stars) fading quickly, where as those produced by short GRBs sources (less massive stars) fading slowly. This really, consistent with fact that supper massive stars burn their fuels (nuclear

reactions) very quickly than less massive stars.

The negative signs of temporal indices (α) characterize all afterglow GRBs decaying following power law model as indicated in figures 4.1 from (a) to (i). Except short GRB090510 with index [(α) = $0.33^{+0.05}_{-0.05}$], the results of analysis show that, the dominant fraction of sampled data consistent with the canonical behaviours: to shallow, normal, and late steep decay phases with temporal indices of [$0.5 < \alpha_2 < 1$], [$1 < \alpha_3 < 1.5$], and [($\alpha_4 \sim 2$)], respectively. Thus among our sampled data:

♦ There are three GRB afterglows: LGRB 130418A, SGRB140903A, and SGRB190627A. They all have temporal indices of (α): $79.^{+0.05}_{-0.05}$, $(0.67^{+0.06}_{-0.06})$, and $(0.63^{+0.04}_{-0.04})$ are in line with the shallow decay phase, respectively, as a result of the central engine's continuous energy injection model to a slowed external shock.

♦ Similarly, three GRBs : (LGRB121128A, LGRB150314A and SGRB051221A) each with temporal indices of : $(1.5^{+0.09}_{-0.09})$, $(1.19^{+0.03}_{-0.03})$, and $(1.17^{+0.07}_{-0.07})$ are consistent with normal decay phase, respectively, as a result of decrease in the Lorentz factor Γ in forward shock and inactive central engine.

♦ The rest two GRBs afterglows: LGRB140614A and LGRB130701A with respective, temporal indices: $1.78^{+0.09}_{-0.09}$ and $1.55^{+0.64}_{-0.64}$, are nearly consistent with late steep decay phase ($\alpha_4 \sim 2$) due to jet breaks and Lorentz factor of the ejecta become larger than θ_0^{-1} compared to the jet opening angle θ_0. In general, $\approx$ 89% of our sampled data fit with the predicted model, except with the early steep decay phase.

Figures 4.1 show, the patterns of each plot is unique, indicating that GRBs are non-repeatable and characterized by diversified light curves. The decaying rate of each X-ray flux aligned with results obtained by calculations.

II. Amplitude (intercept)

♦ Amplitude - the parameter that characterizes X-ray afterglow light curves, and related to the quantity of energy carried by X-ray afterglow, and equivalent to the intensity or the brightness of light curves. It related to energy observed during phase changes. The maximum value of amplitudes, the higher energy observed during initial stage of phase changes from prompt to afterglow.

• In our case, the results of analysis in table 4.1 above, show that $\approx$ 44.4% of the sampled data (almost all LGRBs) have relatively higher amplitude than SGRBs, revealing that, the collapser models emit grater energy than merger models, this is in fact supports the theoretical facts.

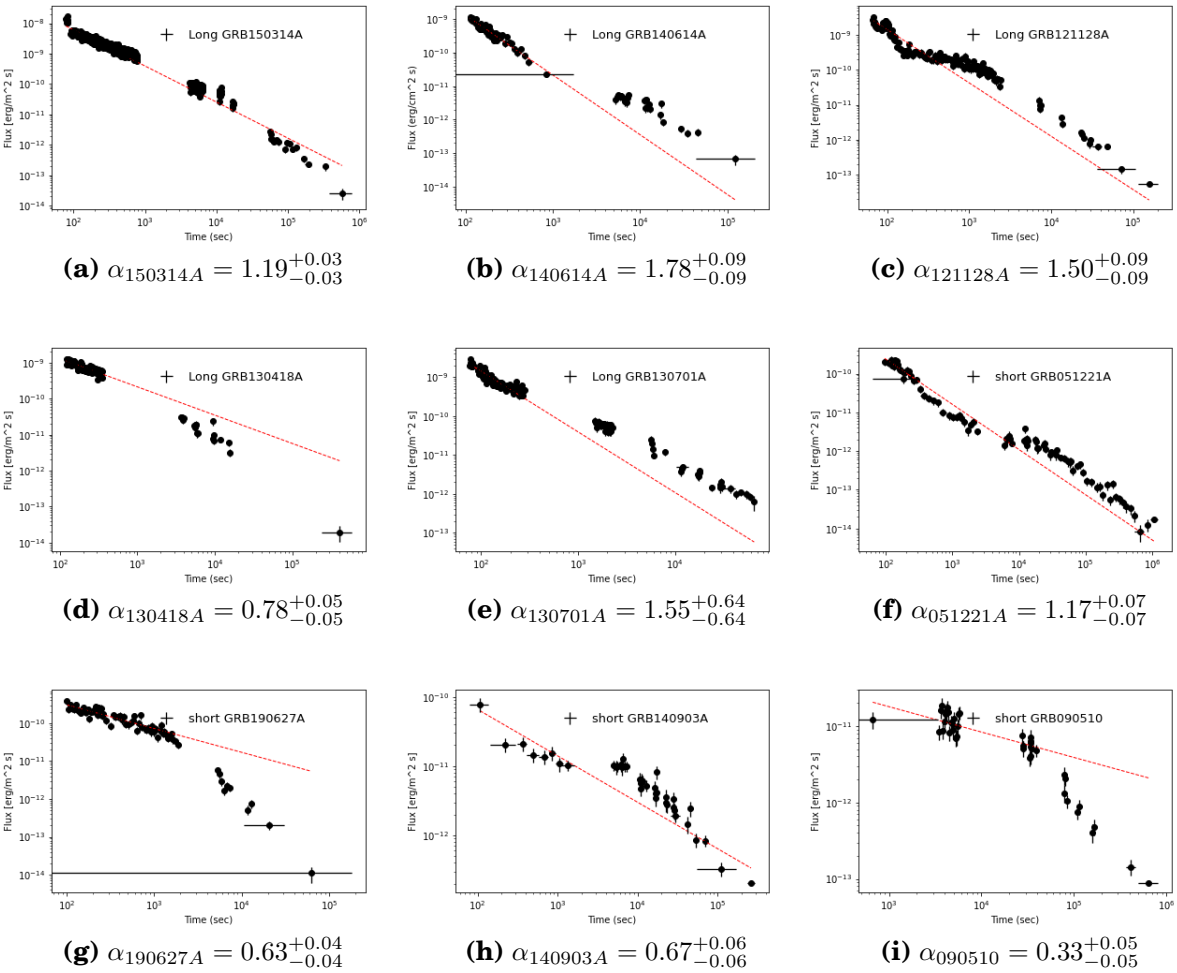

(a) $\alpha_{150314A} = 1.19^{+0.03}_{-0.03}$ **(b)** $\alpha_{140614A} = 1.78^{+0.09}_{-0.09}$ **(c)** $\alpha_{121128A} = 1.50^{+0.09}_{-0.09}$

(d) $\alpha_{130418A} = 0.78^{+0.05}_{-0.05}$ **(e)** $\alpha_{130701A} = 1.55^{+0.64}_{-0.64}$ **(f)** $\alpha_{051221A} = 1.17^{+0.07}_{-0.07}$

(g) $\alpha_{190627A} = 0.63^{+0.04}_{-0.04}$ **(h)** $\alpha_{140903A} = 0.67^{+0.06}_{-0.06}$ **(i)** $\alpha_{090510} = 0.33^{+0.05}_{-0.05}$

Figure 4.1: plots of sampled afterglow GRBs to extract both fitting parameters : indices (α) and amplitudes (A) using jupyter lab programming language.

4.2 Statistical results : R^2, Cov(x,y) and correlation coefficients

Table 4.2 below, comprises the results of statistical analysis : R^2, Cov(x,y) and r_{xy} coefficients that used to explain the distribution of observed points, directional relationship of the variables, and degree of relationship among the sampled data, respectively

. **I. R-squared (R^2) values**

♦ The results of analysis in table 2 above, showed that:

• 67% of the sampled afterglow data, have (R^2) values between 86% - 95%, which is nearest to 1. This result characterizes that, observed points are closer to best fitting line (regression line), which ensured that dependent variable (X-ray flux) completely explained by independent variable, because of continuous energy injection

Table 4.2: Shows various statistical results of data analysed to provide parameters: R^2, Cov(x,y), and correlation coefficients of the sampled data.

GRBYYMMDD	$T_{90}(s)$	z	$Lc_{break(s)}$	$cov(x,y) \times 10^{-8}$	R^2	correl.r_{xy}
GRB140614A	233.90	4.23	2	-20.9	0.95	-1.00
GRB121128A	23.30	2.20	2	-7.06	0.86	-0.99
GRB130418A	>300	1.22	1	-6.18	0.91	-0.99
GRB130701A	4.38	1.16	1	-3.56	0.93	-1.00
GRB150314A	14.79	1.76	1	-0.47	0.83	-0.99
GRB051221A	1.40	0.55	2	-0.12	0.95	-1.00
GRB190627A	1.60	1.94	1	-0.05	0.87	-0.99
GRB090510	0.30	0.90	1	-0.04	0.65	-0.99
GRB140903A	0.30	0.35	1	-0.03	0.81	-0.98

by central engine.

• On the other hand, the rest (33%) of the sampled GRBs afterglow data have R^2 values below 85% (i.e <1), realise that, the observed points are relatively spread away from the best fitting line (red line). This scenario occurred as a result of interaction of ejecta with ISM and time varying of central engine.

II. Covariance C(x,y) and correlation coefficients (r_{xy}).

• The C(x,y) explain the direction movement of the two dimensional data, and helps us to calculate correlation coefficients as well. In table 4.2 below, the value of C(x,y) of all sampled data is negative, revealed that X-ray flux (f) and the emission time (t_{obs}) are moving opposite direction which supports observational and theoretical fact. On the other hand, the results of correlation coefficients r_{xy} showed that:

• 33.3% of the sampled data has r_{xy} = -1.00, indicating that there is perfect negative relationship between the dependent and independent variables, where as,

• 66.7% of the sampled data has $r_{xy} \sim$ -0.98 to $\sim$ -0.99, indicates that there is strong negative relationship between dependent and independent variables.

4.3 Histograms and error bars

Histograms with vertical lines / error bars shown in figures (a) to (i) below, reveal the uncertainty of data point spread about the mean values. From the histogram (f) to (i) above, most of short afterglow samples characterized by long error bars indicate that the observed points are more spread out and thus less reliable, while long afterglow histograms relatively show shorter error bars indicate that the observed points concentrated about the mean , signalling that highly reliable. These phenomena ensure that both events originated from different sources.

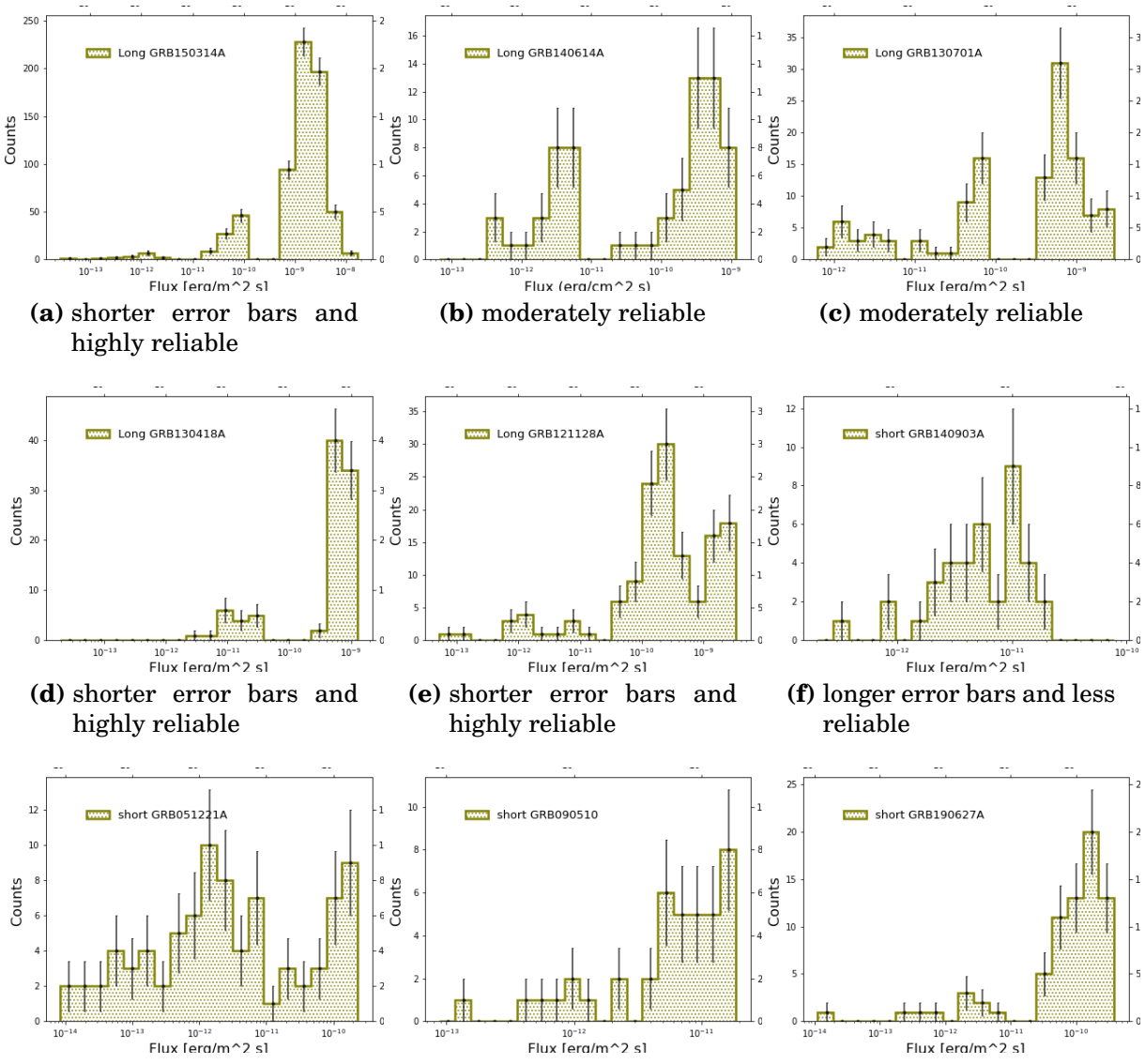

(a) shorter error bars and highly reliable

(b) moderately reliable

(c) moderately reliable

(d) shorter error bars and highly reliable

(e) shorter error bars and highly reliable

(f) longer error bars and less reliable

(g) longer error bars and less reliable

(h) longer error bars and less reliable

(i) longer error bars and less reliable

Figure 4.2: Histograms with the vertical lines / error bars on each, show uncertainty or standard deviations of observed points about the mean value, This is, the results of analysis showing that, short afterglow characterized by long error bars indicates the data spread out the mean value and less reliable. as compared to long afterglows.

CHAPTER 5
Conclusion

Prompt and afterglow are the two stages of gamma-ray bursts. The afterglow phase was anticipated prior to Swift. Nevertheless, until the release of swift, its theoretical and observational understanding was lacking. It was thought to have been produced by photon electrons excited in the external shock arising from the interaction between the relativistic outflows and the surrounding medium at a distance of r $\approx 10^{16}$ - 10^{18} cm from the source. It was distinguished by its multi-wavelength/broken segments and was easily detectable at low energies. According to the theory of afterglow, light curves illustrate how energy dissipates at various emission stages.

In afterglow physics, the canonical X-ray afterglow pictures the initial steep decay $F_x \sim t^{-\alpha}$ with a temporal index [$3 < \alpha_1 < 5$] and an energy spectrum $F_\nu \sim \nu^{-\beta}$ with an energy spectral index [$1 < \beta_1 < 2$] in time interval below the break time. The afterglow light curves rapidly decayed and an important values were in the region of theoretically predicted numerical values. Since the flux decay and the time reading in the X-ray were error oriented, except a few the rest of GRBs were nearly fit to the actual value.

This thesis aims to investigate the phenomenology of GRBs with a particular focus on the canonical behavior of X-ray afterglow light curves. In order to achieve this, nine Swift / XRT data samples with well-defined red shifts (z) and T_{90} were chosen at random. Confirmatory and explanatory research methodologies, pertinent models, and basic statistical tools were all used in our work to analyze the sampled data. As was previously mentioned, the light curves of the majority of canonical X-ray afterglow began to decay as early as 10^2 s after the GRB trigger, with the decaying rate being controlled by a straightforward power law model: $f_\nu \propto t^{-\alpha}$. Each sample's data was analyzed using the Jupyter Lab programming language, and the results were given for interpretation.

• Based on the results of analysis, we have drawn the conclusions, containing five core points:

1) 89% of sampled data consistent with canonical X-ray afterglows of shallow, normal, and late steep decay phases with indices: [0.5 $< \alpha_2 <$ 1.0], [1.0 $< \alpha_3 <$ 1.5], and [$\alpha_4 \sim$ 2], respectively. The former scenario occurred due to continuous energy injection to a decelerated external shocks and a decrease in Lorentz factor Γ in forward shock, while in the second, X-ray flux decaying quickly as a result of active central engine and the last scenario is due to jet breaks.

2) Amplitude - is one of fitting parameter that characterizes X-ray light curves, and related to quantity of energy carried by X-ray. It equivalent to the intensity / brightness of the light curves. The maximum amplitude observed during phase change from prompt to afterglow, that associated with greater energy. In our case, the results of analysis in table 4.1, indicates that $\approx$ 44.4% of the sampled data (almost all LGRBs except one with $T_{90} >$ 300s) have relatively greater amplitude, showing that, LGRBs early afterglows associated with higher energy than SGRBs. Hence, this supports theoretical model.

3) From statistical analysis, the dominant fraction (67%) of sampled data has R^2 values in (%) (86% - 95%), which is nearest to 1, revealing that (X-ray flux) completely explained by the life time of central engine activity. On the other hand, the rest (33%) of the sampled data has R^2 values below 85% (i.e <1), showing that observed points are relatively spread away from the best fitting line. The earlier scenarios were brought about by the central engine's constant energy injection, whereas the later ones were brought about by the interaction between the slowing fireball and the ISM and the Lorentz factor Γ.

4) Covariance C(x,y) and correlation coefficients (r_{xy}) of sampled data. In table 4.2, value of C(x,y) of all sampled data is negative, revealed that, X-ray flux (f) and emission time (t) are moving in opposite directions, that supporting observational and theoretical fact. Furthermore, the results of r_{xy} showed that, r_{xy} of 33.3% of sampled data is exactly -1.00, indicating that there is perfect negative relationship between the variables where as, $r_{xy} \sim$ of 66.7% sample ranges from $\sim$ -0.98 to $\sim$ -0.99, indicating that there is strong negative relationship b/n variables.

5) The longer the lines, the greater spread of observed points around the mean values. As illustrated in histograms, SGRBs afterglow relatively characterized by larger error bars than LGRBs, ensures the two events originated from different progenitor and mechanism as well.

Open problems and potential opportunities

Following the Swift Space Observatory Satellite's launch, the observational and theoretical understanding of the afterglow phase in the historical development of

GRB physics underwent a rapid change. Nonetheless, there are still unanswered questions about the prompt phase's emission mechanism, the engine's lifespan, and how the central engine behaves. In conclusion, I would like to point out the limitations of this thesis work, namely that the obtained findings were limited in their ability to generalize the characteristic of GRB populations due to the smaller sample size of data. This would be resolved in upcoming field research studies.

Bibliography

[1] Piran, Tsvi Gamma-ray burst phyics, *Reviews of Modern Physics, 76 (4), 1143, 2005*

[2] Gomboc, Andreja Unveiling the secrets of gamma ray bursts ,Contemporary Physics , 53 (4), 339–355, 2012

[3] Gehrels, Neil and Ramirez-Ruiz, E and Fox, Derek B Gamma-ray bursts in the Swift era , *Annual Review of Astronomy and Astrophysics, (47), 567–617, 2009.*

[4] Palmerio, Jesse Efficiency of star-generated gamma-ray bursts: Constraints from population models and host galaxies ,2018.

[5] Zhang, Binbin A Multi-wavelength study on gamma-ray bursts and their afterglows, 2011

[6] Dereli, Hüsne Investigation of a Collection of Gamma-ray Bursts with low Afterglows, *arXiv preprint arXiv:1503.04580, 2015*

[7] Hu, You-Dong Multi-wavelength analysis of Fermi and Swift's GRB detection, 2021

[8] Margutti, Raffaella and Zaninoni, E and Bernardini, MG and Chincarini, G A comprehensive statistical analysis of Swift X-ray light-curves: the prompt-afterglow connection in Gamma-Ray Bursts, arXiv preprint arXiv:1207.0537, 2012

[9] Gupta, Rahul and Oates, SR and Pandey, SB and Castro-Tirado, AJ and Joshi, Jagdish C and Hu, YD and Valeev, AF and Zhang, BB and Zhang, Z and Kumar, Amit and others GRB 140102A: insight into prompt spectral evolution and early optical afterglow emission, *Monthly Notices of the Royal Astronomical Society 505 , (3), 4086–4105 2021.*

[10] Moneer, Eman Spectral study of GRBs detected by the Swift and Fermi satellites ,2019

[11] Massaro, Francesco and Thompson, David J and Ferrara, Elizabeth C The extragalactic gamma-ray sky in the Fermi era, The Astronomy and Astrophysics Review, 24,(1), 2, 2016.

[12] Cenko, S Bradley Short-Duration Gamma-Ray Bursts: A Primer, 2018

[13] Knust, Fabian Applying the Fireball Model to Short Gamma-Ray Burst Afterglows: Methods, Jet Opening Angles and Plateau Phases, 2017

[14] Dainotti, MG and Del Vecchio, Roberta Gamma Ray Burst afterglow and prompt-afterglow relations: An overview,*New Astronomy Reviews, 77, 23–61, 2017*

[15] Vedrenne, Gilbert and Atteia, Jean-Luc Gamma-ray bursts: The brightest explosions in the universe,2009

[16] Turpin, D and Heussaff, V and Dezalay, J-P and Atteia, JL and Klotz, A and Dornic, D Connecting Prompt and Afterglow GRB emission I. Investigating the impact of optical selection effects in the Epi-Eiso plane arXiv preprint arXiv:1503.02760, 2015

[17] Piran, Tsvi Gamma-ray bursts and the fireball model, *Physics Reports, 314, (6), 575–667, 1999.*

[18] Kumar, Pawan and Zhang, Bing The physics of relativistic jets and gamma-ray bursts, Physics Reports, 561, 1–109, 2015

[19] Sokolov, VV and Bisnovatyi-Kogan, GS and Kurt, VG and Gnedin, Yu N and Baryshev, Yu V Observational constraints on the angular and spectral distributions of photons in gamma-ray burst sources Astronomy reports, 50, 612–625 , 2006.

[20] Piran, Tsvi A Brief Overview of Magnetic Fields in Gamma-Ray Bursts: AIP Conference Proceedings, 784, (1), 164–174, 2005.

[21] Lipunov, Vladimir and Simakov, Sergey and Gorbovskoy, Evgeny and Vlasenko, Daniil Smooth optical self-similar emission of gamma-ray bursts,*The Astrophysical Journal, 845 , (1), 25, 2017.*

[22] PeEr, Asaf Physics of gamma-ray bursts prompt emission, Advances in Astronomy, 2015, 2015.

[23] Ukwatta, Tilan N Spectral lags and variability of Gamma-ray Bursts in the Swift era, 201

[24] Podsiadlowski, Philipp and Oswalt, TD and Barstow, MA Supernovae and gamma ray burst Planets, Stars and Stellar Systems. Volume 4: *Stellar Structure and Evolution, 4 , 693, 2013.*

[25] Dar, Arnon and De Rujula, Alvaro Towards a comprehensive theory of gamma-ray bursts, Physics Reports, 405, 203–278 (2004).

[26] Fargion, Daniele and Oliva, Pietro Solving the missing GRB neutrino and GRB-SN puzzles ,Nuclear and particle physics proceedings , 297, 249–258, 2018.

[27] Mazzali, Paolo A and Kawabata, Koji S and Maeda, Keiichi and Nomoto, Ken'ichi and Filippenko, Alexei V and Ramirez-Ruiz, Enrico and Benetti, Stefano and Pian, Elena and Deng, Jinsong and Tominaga, Nozomu and others An asymmetric energetic type Ic supernova viewed off-axis, and a link to gamma ray bursts, Science, 308, (5726), 1284–1287 ,2005.

[28] Dirirsa, Feraol Fana Gamma-ray bursts as probes of cosmological parameters at high redshifts, 2018.

[29] Salaris, Maurizio and Cassisi, Santi Evolution of stars and stellar populations,2005

[30] Gao, He and Wu, Xue-Feng and Mészáros, Peter Cosmic transients test Einstein's equivalence principle out to GeV energies, The Astrophysical Journal, 810, (2), 21, 2015.

[31] Yi, Shuang-Xi and Xie, Wei and Ma, Shuai-Bing and Lei, Wei-Hua and Du, Mei Constraining properties of GRB central engines with X-ray flares, *Monthly Notices of the Royal Astronomical Society ,507, (1), 1047–1054, 2021.*

[32] Willingale, R and O'brien, PT and Osborne, JP and Godet, O and Page, KL and Goad, MR and Burrows, DN and Zhang, B and Rol, E and Gehrels, N and others Testing the standard fireball model of gamma-ray bursts using late X-ray afterglows measured by Swift, The Astrophysical 662 (2) , 1093, 2007.

[33] Piran, Tsvi Resolving the mystery of Gamma-Ray Bursts: Physics Reports, 333, 529–553, 2000.

[34] Dermer, Charles D Curvature effects in gamma-ray burst colliding shells, *The Astrophysical Journal, 614, (1), 284), 2004.*

[35] Del Vecchio, Roberta New study of afterglow light curves in gamma ray bursts, 2018.

[36] HESS collaboration and Abdalla, H and Aharonian, F and Ait Benkhali, F and Angüner, EO and Arcaro, C and Armand, C and Armstrong, T and Ashkar, H and Backes, M and others Revealing x-ray and gamma ray temporal and spectral similarities in the GRB 190829A afterglow, Science, 372, (6546), 1081–1085, 2021.

[37] Fan, YZ and Wei, DM Late internal-shock model for bright X-ray flares in gamma-ray burst afterglows and GRB 011121, Monthly Notices of the Royal Astronomical Society: Letters,364, (1), L42–L46, 2005.

[38] Fan, Yizhong and Piran, Tsvi Gamma-ray burst efficiency and possible physical processes shaping the early afterglow, *Monthly Notices of the Royal Astronomical Society, 369, 1, 197–206, 2006.*

[39] Mangano, Vanessa and La Parola, Valentina and Cusumano, Giancarlo and Mineo, Teresa and Malesani, Daniele and Dyks, Jaroslaw and Campana, Sergio and Capalbi, Milvia and Chincarini, Guido and Giommi, Paolo and others Swift XRT observations of the afterglow of XRF 050416A, The Astrophysical Journal, 654,(1), 403, 2007.

[40] Ramirez-Ruiz, Enrico and Dray, Lynnette M and Madau, Piero and Tout, Christopher A Winds from massive stars: consequences for γ-ray burst afterglows,*Monthly Notices of the Royal Astronomical Society, 327, 3, 829–840, 2001.*

*[41] Lee, Chang-Hwan and Brown, Gerald E On the theory of gamma ray bursts and hypernovae: The black hole soft X-ray transient sources,*International Journal of Modern Physics A, 18, 04, 527–576, 2003.

[42] Rees, Martin J and Mészáros, Péter Dissipative photosphere models of gamma-ray bursts and X-ray flashes, *The Astrophysical Journal, 628, 2, 847, 2005.*

[43] Granot, Jonathan and Sari, Re'em The shape of spectral breaks in gamma-ray burst afterglows, The Astrophysical Journal, 568, (2), 820, 2002.

[44] Ghisellini, G and Ghirlanda, G and Nava, L and Firmani, C "Late Prompt" emission in gamma-ray bursts?, The Astrophysical Journal, 658, (2), L75, 2007.

[45] Wijers, RAMJ and Galama, TJ Physical parameters of GRB 970508 and GRB 971214 from their afterglow synchrotron emission, *The Astrophysical Journal, 523, (1), 177, 1999*

[46] Levan, Andrew Gamma-ray bursts, 2018

[47] Zhang, Bing and Lü, Hou-Jun and Liang, En-Wei GRB observational properties, Space Science Reviews, 202, 3–32, 2016

[48] Virgili, Francisco J Gamma-ray burst populations

[49] Bloom, Joshua S What are gamma-ray bursts?, 2, 2011.

[50] Levan, Andrew J Gamma-ray bursts and their environments, 2005.

[51] Vergani, Susanna D Studies on the gamma-ray burst phenomenon and on its use to probe the high redshift universe, 2009

[52] Selsing, Jonatan Illuminating the dark: with cosmic explosions and their afterglows Ph. D. Thesis, 2018

[53] Covino, Stefano and Gotz, Diego Polarization of prompt and afterglow emission of Gamma-Ray Bursts, Covino, Stefano and Gotz, Diego, *arXiv preprint arXiv:1605.03588, 2016*

[54] Beloborodov, AM and Mészáros, P Photospheric emission of gamma-ray bursts, Space Science Reviews 207, 87–110, 2017.

[55] Eid, Hala A Probing GRB environments through x-ray absorption, 2008.

DECLARATION

ADDIS ABABA UNIVERSITY
COLLEGE OF NATURAL AND COMPUTATIONAL SCIENCES
DEPARTMENT OF PHYSICS

MSc Thesis

Light Curve Characteristic of Gamma-Ray Burst

Name of Candidate: Temam Beyan

I the under signed declare that the thesis is my original work and no part of it can be claimed as an intellectual property of anybody else except me and my advisors.

Signature: _____